Cell Metabolism
Article

The FBXL5-IRP2 Axis Is Integral to Control of Iron Metabolism In Vivo

Toshiro Moroishi,[1,2] Masaaki Nishiyama,[1,2] Yukiko Takeda,[2,3] Kazuhiro Iwai,[2,3] and Keiichi I. Nakayama[1,2,*]
[1]Department of Molecular and Cellular Biology, Medical Institute of Bioregulation, Kyushu University, 3-1-1 Maidashi, Higashi-ku, Fukuoka, Fukuoka 812-8582, Japan
[2]CREST, Japan Science and Technology Agency (JST), Kawaguchi, Saitama 332-0012, Japan
[3]Department of Biophysics and Biochemistry, Graduate School of Medicine, and Cell Biology and Metabolism Group, Graduate School of Frontier Biosciences, Osaka University, Suita, Osaka 565-0871, Japan
*Correspondence: nakayak1@bioreg.kyushu-u.ac.jp
DOI 10.1016/j.cmet.2011.07.011

SUMMARY

Iron-dependent degradation of iron-regulatory protein 2 (IRP2) is a key event for maintenance of an appropriate intracellular concentration of iron. Although FBXL5 (F box and leucine-rich repeat protein 5) is thought to mediate this degradation, the role of FBXL5 in the control of iron homeostasis in vivo has been poorly understood. We have now found that mice deficient in FBXL5 died in utero, associated with excessive iron accumulation. This embryonic mortality was prevented by additional ablation of IRP2, suggesting that impaired IRP2 degradation is primarily responsible for the death of *Fbxl5*$^{-/-}$ mice. We also found that liver-specific deletion of *Fbxl5* resulted in deregulation of both hepatic and systemic iron homeostasis, leading to the development of steatohepatitis. The liver-specific mutant mice died with acute liver failure when fed a high-iron diet. Thus, our results uncover a major role for FBXL5 in ensuring an appropriate supply of iron to cells.

INTRODUCTION

Iron is an essential cofactor for many proteins that function in oxygen transport, cellular respiration, or DNA synthesis (Rouault and Tong, 2005), with iron deficiency resulting in cellular growth arrest and death. Conversely, the chemical properties of iron give rise to side reactions that damage macromolecules (Hentze et al., 2010). Thus, excess ferrous iron reacts with hydrogen peroxide or lipid peroxides to generate hydroxyl and lipid radicals, respectively. These oxygen metabolites react readily with biological molecules including proteins, lipids, and DNA. Given that both iron deficiency and iron overload are deleterious to cells, defects in iron acquisition at the cellular and systemic levels lead to human disorders (De Domenico et al., 2008). Thus, iron homeostasis is strictly controlled to ensure provision of a proper amount of iron to cells.

The control of systemic iron homeostasis occurs through regulation of iron acquisition (Andrews and Schmidt, 2007), given that iron loss occurs only through exfoliation and blood loss. Plasma iron levels are determined predominantly by the amount of duodenal iron absorption and by iron release from macrophages that recycle iron from senescent red blood cells (Wang and Pantopoulos, 2011). These iron fluxes are precisely regulated by hepcidin, a small peptide hormone released from the liver that is also known as Hamp1 or Leap1. Hepcidin negatively regulates iron transport into plasma by controlling the expression of an iron exporter, ferroportin (Nemeth et al., 2004). Thus, systemic iron metabolism is maintained in balance by the hepcidin-ferroportin regulatory system.

At the cellular level, iron homeostasis is regulated by coordination of iron uptake, storage, export, and utilization (Hentze et al., 2010). Iron is imported into cells in the ferrous form and accumulates as a cytosolic labile iron pool (LIP) that is essential for direct incorporation of iron into proteins or for its transport into mitochondria, which constitute a major site of iron utilization. Ferrous iron from the LIP that is not utilized for metalation reactions is exported by ferroportin or stored in a redox-inactive form (ferric iron) bound to ferritin, thereby preventing iron-mediated cell damage. Thus, the size of the LIP is determined by the rates of iron uptake, storage, export, and utilization, and these processes must be strictly regulated to prevent deleterious iron deficiency or excess.

The abundance of some proteins that contribute to determination of the size of the LIP is regulated at the posttranscriptional level by iron-regulatory protein 1 (IRP1) and IRP2 (Muckenthaler et al., 2008). These RNA-binding proteins interact with conserved *cis*-regulatory hairpin structures known as iron-responsive elements (IREs) during iron-limiting conditions to regulate the translation and stability of mRNAs that encode proteins required for iron homeostasis. IRP1 (but not IRP2) is a bifunctional protein: in the apo-IRP1 form, it binds to IREs and thereby controls gene expression; however, it also assembles to form a [4Fe-4S] cluster that does not bind IREs and thereby becomes cytosolic aconitase (holo-IRP1) under iron-sulfur cluster-replete conditions. Both apo-IRP1 and IRP2 inhibit initiation of translation when they are bound to IREs in the 5′ untranslated regions of mRNAs for the H or L chains of ferritin (which mediate iron storage), for ferroportin (which mediates iron export), or for aminolevulinic acid synthase 2 (Alas2, which mediates iron utilization), whereas their binding to the IRE in the 3′ untranslated region of the mRNA for transferrin receptor 1 (TfR1, which mediates iron uptake) prevents its degradation.

As a consequence of these interactions, IRPs increase the size of the LIP (ferrous iron) during iron-limiting conditions. In contrast, under iron-replete conditions, IRPs are degraded by the proteasome, leading to a decrease in the size of the cytosolic LIP. Thus, iron-dependent degradation of IRPs in iron-replete cells is a key event in the maintenance of an appropriate intracellular concentration of iron.

An iron- and oxygen-regulated SCF-type ubiquitin ligase (E3), SCF^{FBXL5}, has been shown to contribute to iron-dependent degradation of IRP1 and IRP2 (Salahudeen et al., 2009; Vashisht et al., 2009). FBXL5 (F box and leucine-rich repeat protein 5) is a member of the F box family of proteins that confer substrate specificity on SCF-type ubiquitin ligases (Jin et al., 2004; Nakayama and Nakayama, 2006). FBXL5 contains a unique hemerythrin domain that is related to a family of iron- and oxygen-binding proteins in bacteria and invertebrates. Direct binding of iron to the hemerythrin domain stabilizes FBXL5, which is unstable under iron-deficient conditions. Thus, such binding results in the degradation of IRPs by the stabilized FBXL5 under iron-replete conditions. However, despite its integral role in IRP degradation, the biological relevance of FBXL5 as well as its effects on iron homeostasis have remained unknown.

We have now inactivated the mouse FBXL5 gene globally and selectively. Our characterization of these FBXL5-deficient mice has revealed that FBXL5 plays a pivotal role in the maintenance of appropriate concentrations of intracellular iron and that it is essential both for embryonic development and for normal postnatal liver physiology. Loss of FBXL5 in mice induced apoptosis as a result of unrestrained IRP activity, and consistent with this finding, deletion of *Irp2* in $Fbxl5^{-/-}$ mice prevented their embryonic death. Our results indicate that the FBXL5-IRP2 axis is integral to iron homeostasis in vivo.

RESULTS

Loss of FBXL5 Results in Embryonic Mortality in Mice

To elucidate the physiological functions of FBXL5, we generated mice deficient in this protein. The FBXL5 gene was disrupted in mouse embryonic stem cells (ESCs) by replacement of exons 4 and 5, which encode the F box domain, with IRES-*lacZ* and PGK-*neo*-poly(A)-loxP cassettes (see Figure S1 available online). Mice heterozygous for the *Fbxl5* mutant allele were healthy, fertile, and phenotypically indistinguishable from wild-type littermates. In contrast no homozygous mutants were detected among 372 newborn animals generated from heterozygote crosses, even though the ratio of wild-type to heterozygous offspring was normal (Figure 1A). Thus, the mutation appeared to be embryonic lethal in the homozygous state. Whole-mount in situ hybridization analysis revealed that FBXL5 mRNA was present throughout wild-type embryos from embryonic day (E) 7.5 to E8.5 but that it was localized predominantly in the brain from E9.5 to E11.5 (Figure 1B). No hybridization signal was detected in $Fbxl5^{-/-}$ embryos (Figure 1C).

To determine the time at which the *Fbxl5* mutation becomes lethal, we examined embryos from $Fbxl5^{+/-}$ intercrosses at various developmental stages (Figure 1A). Most $Fbxl5^{-/-}$ embryos underwent resorption manifesting growth retardation and massive hemorrhage at E8.5 and thereafter, although the mutant embryos appeared normal at E7.5 (Figure 1D). Histopathologic examination revealed that $Fbxl5^{+/-}$ and $Fbxl5^{-/-}$ embryos were indistinguishable at E7.5, with each egg cylinder consisting of three layers of tissue (ectoderm, mesoderm, and visceral endoderm) (Figure 1E). However, $Fbxl5^{-/-}$ embryos manifested growth retardation and were inviable at E8.5. Apoptotic cells with condensed nuclei as well as hemorrhage in the region of the ectoplacental cone were typically observed in the $Fbxl5^{-/-}$ embryos. Thus, these results suggested that FBXL5 is essential for early embryonic development.

Fatal Iron Accumulation in $Fbxl5^{-/-}$ Embryos

To explore the cause of the abnormal cell death observed in the ectoplacental cone of $Fbxl5^{-/-}$ embryos, we performed diaminobenzidine (DAB)-enhanced Perls staining and DAB-enhanced Turnbull staining, which are specific for ferric and ferrous iron, respectively (Meguro et al., 2003) (Figure 2A). Both Perls- and Turnbull-positive iron deposits were observed in the ectoplacental cone of $Fbxl5^{-/-}$ embryos at E8.5, suggesting that ferrous iron accumulated in these embryos. Furthermore, ferrous iron deposits were also observed in the extraembryonic visceral endoderm of $Fbxl5^{-/-}$ embryos at E7.5, before morphological changes were apparent.

The extraembryonic visceral endoderm and the ectoplacental cone function as an early placenta in maternoembryonic nutrient transport before formation of the placenta proper (Cross et al., 1994). Given that iron is supplied to the embryo through this early placenta, we hypothesized that the loss of FBXL5 might result in iron overload in the early placenta, leading to oxidative stress. A marked increase in the abundance of cytoplasmic 4-hydroxy-2-nonenal (4-HNE)-modified proteins, an indicator of oxidative stress, was apparent as early as E7.5 in the extraembryonic visceral endoderm of $Fbxl5^{-/-}$ embryos, compared with that in $Fbxl5^{+/-}$ embryos (Figure 2B). Although the TUNEL (terminal deoxynucleotidyl transferase-mediated dUTP nick-end labeling) assay did not detect apoptotic cells at E7.5 (Figure S2A), several apoptotic cells were apparent in the ectoplacental cone as well as in the embryonic portion of $Fbxl5^{-/-}$ embryos at E8.5 (Figure 2C). These results suggested that the loss of FBXL5 results in iron overload, leading to oxidative stress and apoptosis, in the early embryo.

To assess directly the growth capability of $Fbxl5^{-/-}$ embryos independent of placental function, we examined the outgrowth of blastocysts in culture. All $Fbxl5^{+/+}$, $Fbxl5^{+/-}$, and $Fbxl5^{-/-}$ blastocysts hatched, attached to the culture dish, and produced apparently normal trophoblast giant cells and an inner cell mass under normal iron conditions (Figure S2B), suggesting that $Fbxl5^{-/-}$ blastocysts develop normally in the absence of iron stress. However, under high-iron conditions, development of both the trophectoderm and inner cell mass by $Fbxl5^{-/-}$ blastocysts was impaired, with this impairment being prevented by the presence of the antioxidant *N*-acetyl-L-cysteine (NAC) (Figure 2D). Thus, these observations indicated that not only the early placenta but also embryonic tissue is damaged by iron overload and consequent oxidative stress in the absence of FBXL5.

IRP Accumulation in FBXL5-Deficient Mice

Given that iron accumulation was observed in $Fbxl5^{-/-}$ embryos, we hypothesized that upregulation of IRPs might be

A

Embryonic day	No. of animals recoverable			Total no. of animals
	Fbxl5$^{+/+}$	*Fbxl5*$^{+/-}$	*Fbxl5*$^{-/-}$ (no. resorbed)	
E3.5	3	12	6 (0)	21
E7.5	18	29	9 (0)	56
E8.5	11	19	4 (4)	34
E9.5	4	17	7 (7)	28
E11.5	8	14	8 (8)	30
E13.5	15	33	12 (12)	60
Newborn	132	240	0 (0)	372

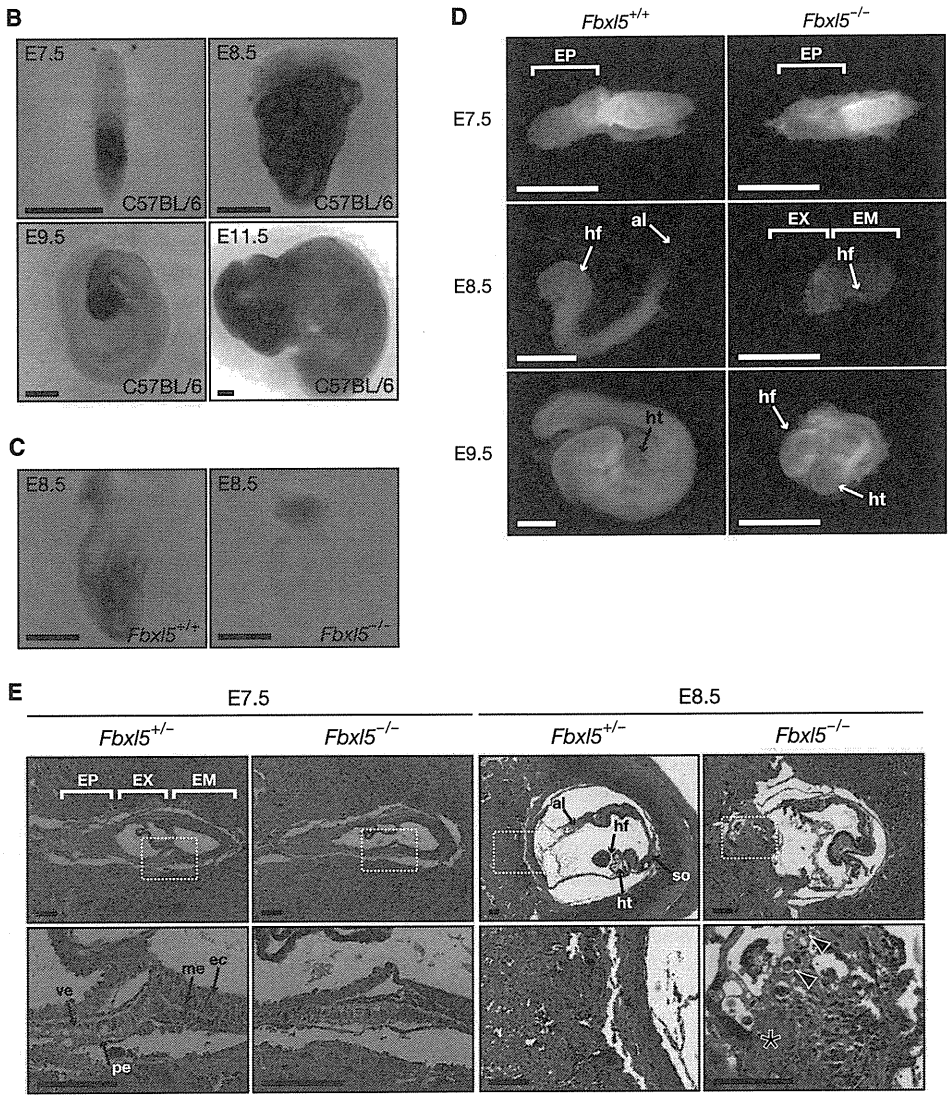

Figure 1. Targeted Disruption of *Fbxl5* Results in Embryonic Death

(A) Genotype frequencies for total embryos and live offspring produced from *Fbxl5*$^{+/-}$ mouse intercrosses. Numbers in parentheses indicate resorbed embryos.

(B) Whole-mount in situ hybridization of C57BL/6 embryos at E7.5, E8.5, E9.5, and E11.5 with a riboprobe specific for FBXL5 mRNA. Scale bars, 500 μm.

(C) Whole-mount in situ hybridization of *Fbxl5*$^{+/+}$ and *Fbxl5*$^{-/-}$ embryos at E8.5 with an FBXL5 riboprobe. Scale bars, 500 μm.

(D) Gross appearance of *Fbxl5*$^{+/+}$ versus *Fbxl5*$^{-/-}$ embryos at E7.5, E8.5, and E9.5. EP, ectoplacental cone; EX, extraembryonic portion; EM, embryonic portion; hf, headfold; al, allantois; ht, heart. Scale bars, 500 μm.

(E) Histopathology of *Fbxl5*$^{-/-}$ embryos. The development of *Fbxl5*$^{+/-}$ and *Fbxl5*$^{-/-}$ embryos is shown at E7.5 and E8.5. The boxed regions in the upper panels are shown at higher magnification in the lower panels. Apoptotic cells with condensed nuclei (arrowheads) as well as hemorrhage and fibrin (asterisk) in the area of the ectoplacental cone are indicated. ec, ectoderm; me, mesoderm; pe, parietal endoderm; ve, visceral endoderm; so, somites. Scale bars, 100 μm. See also Figure S1.

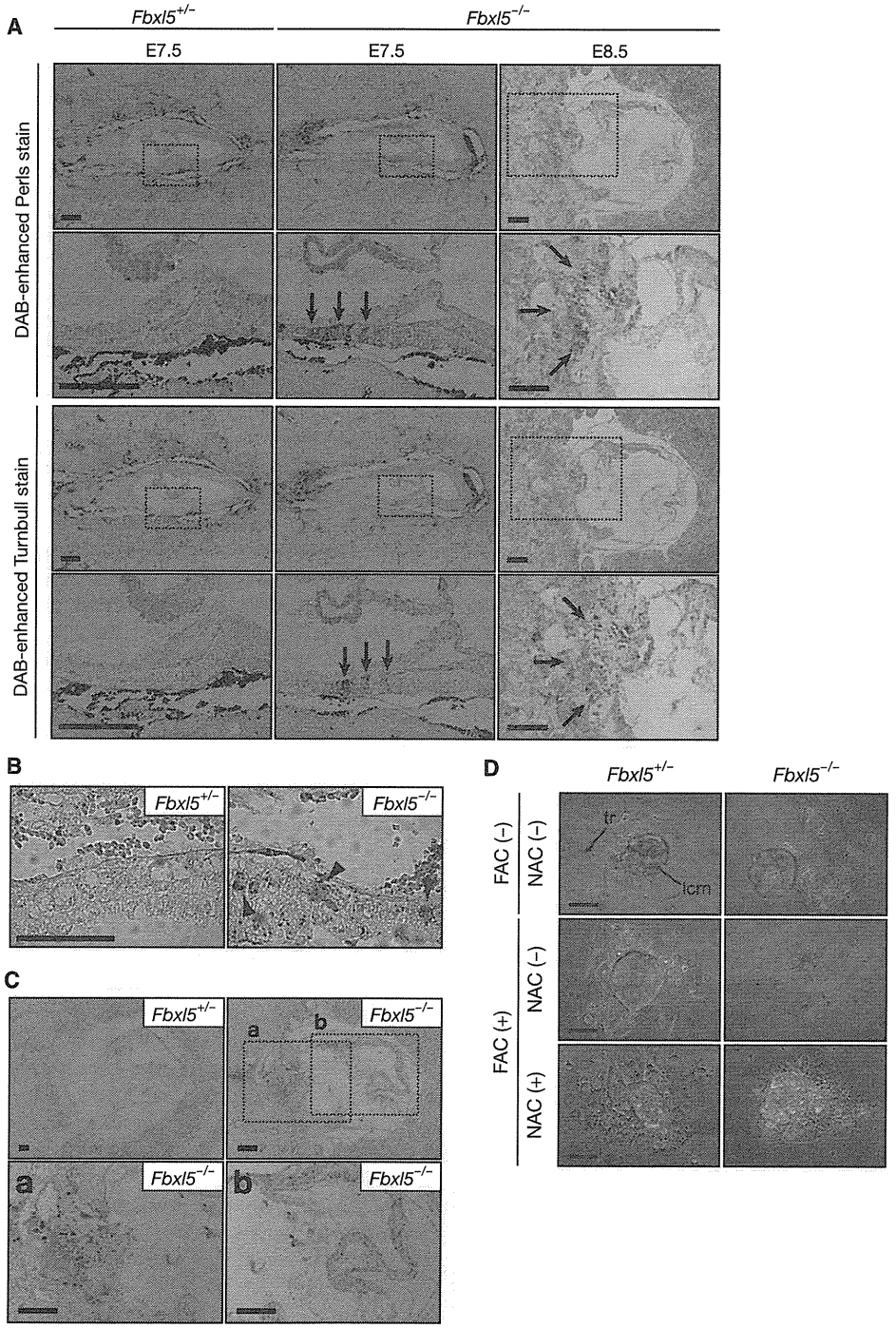

Figure 2. Fatal Iron Accumulation and Oxidative Stress in *Fbxl5*$^{-/-}$ Embryos

(A) DAB-enhanced Perls staining (top panels) and DAB-enhanced Turnbull staining (bottom panels) of *Fbxl5*$^{+/-}$ (E7.5) and *Fbxl5*$^{-/-}$ (E7.5 and E8.5) embryos. The boxed regions in the upper panels of each set are shown at higher magnification in the lower panels. Brown staining indicates iron accumulation in the extra-embryonic visceral endoderm (E7.5) or ectoplacental cone (E8.5) of *Fbxl5*$^{-/-}$ embryos (arrows). Scale bars, 100 μm.

(B) Sections of *Fbxl5*$^{+/-}$ and *Fbxl5*$^{-/-}$ embryos at E7.5 were subjected to immunohistochemical staining with antibodies to 4-HNE. Arrowheads indicate an increased staining intensity for 4-HNE-modified proteins in the extraembryonic visceral endoderm of the *Fbxl5*$^{-/-}$ embryo. Scale bar, 50 μm.

(C) Sections of *Fbxl5*$^{+/-}$ and *Fbxl5*$^{-/-}$ embryos at E8.5 were subjected to the TUNEL assay. Higher-magnification views of the ectoplacental cone (a) and embryonic portion (b) of the *Fbxl5*$^{-/-}$ embryo are also shown. Scale bars, 100 μm.

(D) Blastocysts from *Fbxl5*$^{+/-}$ mouse intercrosses were cultured in the absence or presence of ferric ammonium citrate (FAC, 50 μg/ml) or NAC (1 mM) for 5 days in vitro. The development of *Fbxl5*$^{+/-}$ and *Fbxl5*$^{-/-}$ blastocysts was examined at E8.5. icm, inner cell mass; tr, trophectoderm. Scale bars, 100 μm. See also Figure S2.

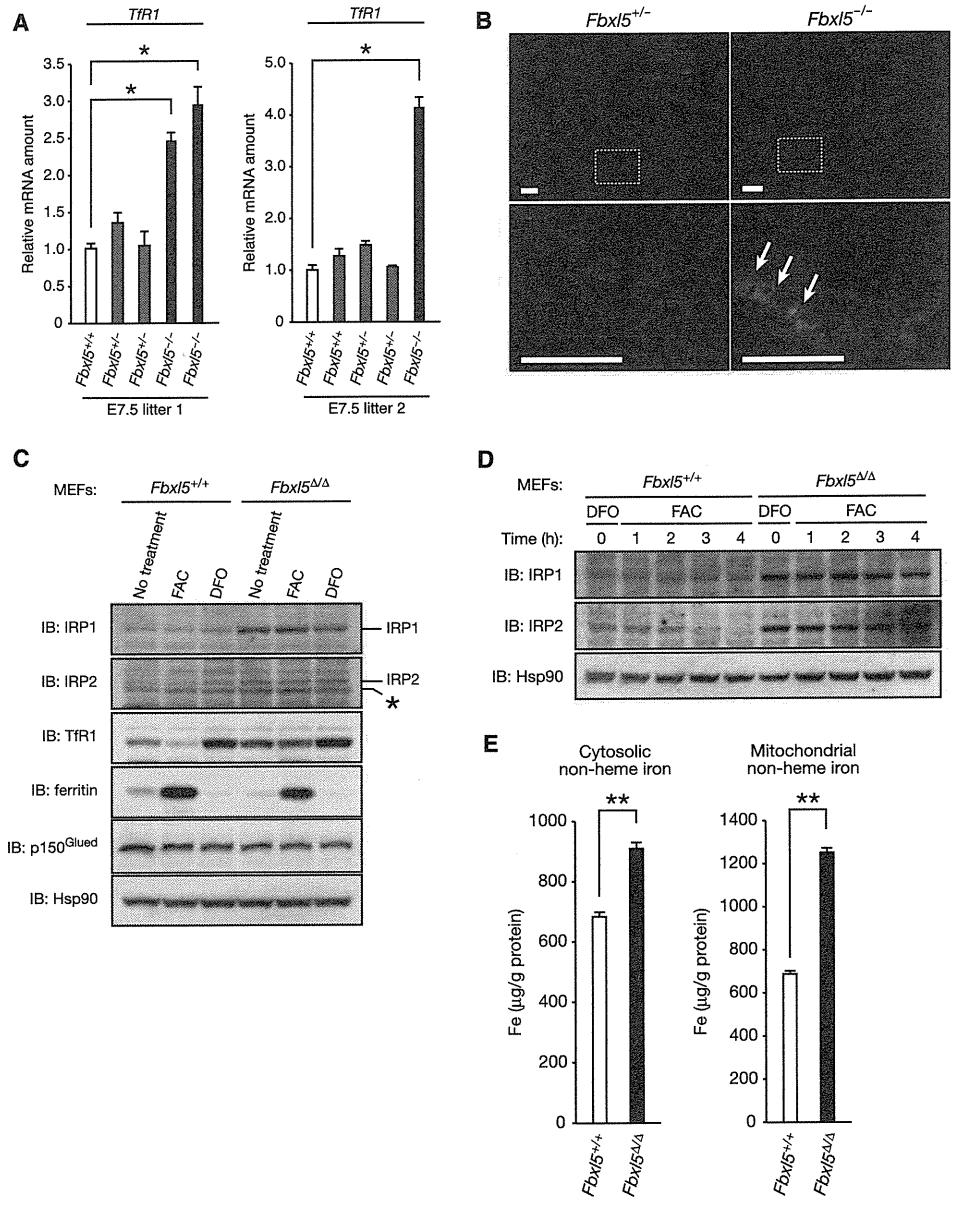

Figure 3. Accumulation of IRPs in FBXL5-Deficient Mice

(A) RT and real-time PCR analysis of TfR1 mRNA in littermate embryos of *Fbxl5*$^{+/-}$ mouse intercrosses at E7.5. Normalized data are expressed relative to the corresponding value for a control *Fbxl5*$^{+/+}$ embryo and are mean ± SEM from three independent experiments. *$p < 0.03$ (Student's t test).

(B) Sections of *Fbxl5*$^{+/-}$ and *Fbxl5*$^{-/-}$ embryos at E7.5 were subjected to immunohistofluorescence analysis with antibodies to TfR1. The boxed regions in the upper panels are shown at higher magnification in the lower panels. Arrows indicate an increased staining intensity for TfR1 in the extraembryonic mesoderm of the *Fbxl5*$^{-/-}$ embryo. Scale bars, 50 μm.

(C) *Fbxl5*$^{+/+}$ or *Fbxl5*$^{\Delta/\Delta}$ MEFs were incubated for 16 hr in the absence or presence of FAC (100 μg/ml) or 100 μM of the ferric-iron chelator desferrioxamine (DFO) and were then subjected to immunoblot (IB) analysis with antibodies to the indicated proteins. The asterisk indicates a nonspecific band.

(D) Immunoblot analysis of IRP1 and IRP2 in cells exposed to iron. *Fbxl5*$^{+/+}$ or *Fbxl5*$^{\Delta/\Delta}$ MEFs were incubated for 16 hr with 100 μM DFO and then exposed to FAC (50 μg/ml) for the indicated times.

(E) Total nonheme iron levels in cytosolic and mitochondrial fractions prepared from *Fbxl5*$^{+/+}$ or *Fbxl5*$^{\Delta/\Delta}$ MEFs that had been exposed to FAC (100 μg/ml) for 48 hr. Data are mean ± SD from three independent experiments. **$p < 0.01$ (Student's t test). See also Figure S3.

responsible for this deregulation of iron homeostasis. Therefore, we examined the abundance of TfR1 mRNA, a downstream target of IRPs, in the mutant embryos. The amount of TfR1 mRNA was markedly increased in *Fbxl5*$^{-/-}$ embryos (Figure 3A). Immunostaining also revealed that TfR1 accumulated in the extraembryonic mesoderm of *Fbxl5*$^{-/-}$ embryos at E7.5 (Figure 3B). Thus, these results suggested that IRP activity is increased, resulting in deregulation of IRP target genes, in *Fbxl5*$^{-/-}$ embryos.

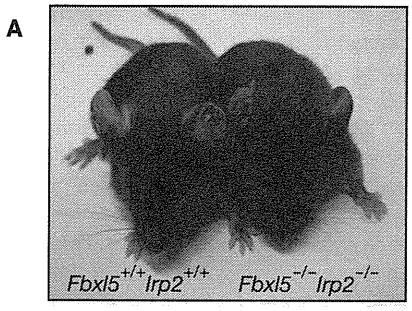

B

	No. of animals			
	Irp2$^{+/+}$	*Irp2*$^{+/-}$	*Irp2*$^{-/-}$	Total
Fbxl5$^{+/+}$	22	37	13	72
Fbxl5$^{+/-}$	48	95	32	175
Fbxl5$^{-/-}$	0	0	19	19
Total	70	132	64	266

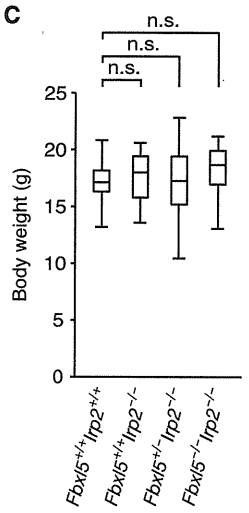

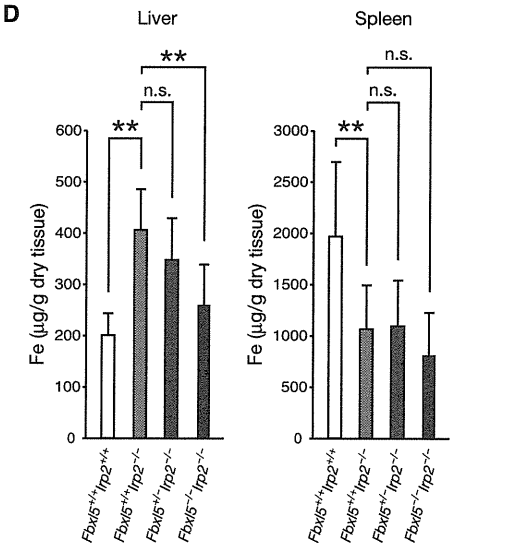

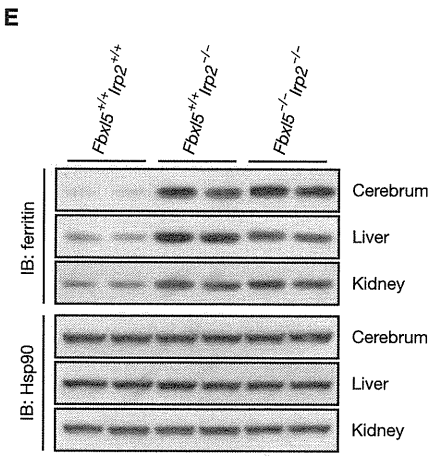

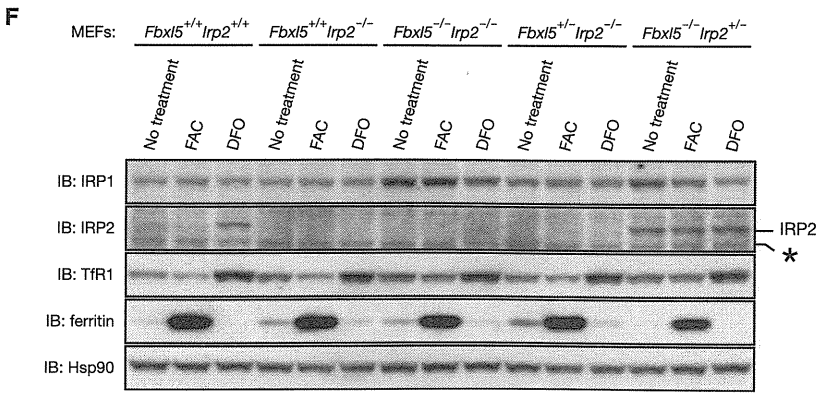

Figure 4. Prevention of Embryonic Mortality in FBXL5-Deficient Mice by Ablation of IRP2

(A) Gross appearance of *Fbxl5*$^{+/+}$*Irp2*$^{+/+}$ versus *Fbxl5*$^{-/-}$*Irp2*$^{-/-}$ littermates at 5 weeks of age.

(B) Genotype frequencies of 4-week-old mice produced from *Fbxl5*$^{+/-}$*Irp2*$^{+/-}$ mouse intercrosses.

(C) Box plot with whiskers from minimum to maximum body weight in *Fbxl5*$^{+/+}$*Irp2*$^{+/+}$ (n = 22), *Fbxl5*$^{+/+}$*Irp2*$^{-/-}$ (n = 10), *Fbxl5*$^{+/-}$*Irp2*$^{-/-}$ (n = 26), and *Fbxl5*$^{-/-}$*Irp2*$^{-/-}$ (n = 15) mice at 4 weeks of age. n.s., not significant ($p > 0.05$, Student's t test).

The early embryonic mortality of the *Fbxl5*$^{-/-}$ mutant impeded in-depth analysis of the role of FBXL5 in iron homeostasis. To overcome this obstacle, we generated mice in which *Fbxl5* is conditionally ablated in a tissue-specific manner. To this end, we first produced mice harboring a "floxed" allele of *Fbxl5*, in which exons 4 and 5 are flanked by loxP sites (Figures S3A–S3C). Mice homozygous for the floxed *Fbxl5* allele (*Fbxl5*$^{F/F}$ mice) had no apparent defects, indicating that the allele is fully functional.

To investigate whether iron-dependent degradation of IRPs is impaired in FBXL5-deficient mice, we prepared mouse embryonic fibroblasts (MEFs) from *Fbxl5*$^{+/+}$ and *Fbxl5*$^{F/F}$ embryos at E13.5 and subsequently infected these cells with a retroviral vector encoding Cre recombinase. We confirmed that almost all floxed alleles were deleted by Cre recombinase in the MEFs from *Fbxl5*$^{F/F}$ embryos, giving rise to *Fbxl5*$^{\Delta/\Delta}$ MEFs (Figure S3D). Immunoblot analysis revealed that the abundance of IRP1 and IRP2 was increased in *Fbxl5*$^{\Delta/\Delta}$ MEFs, whereas that of the other potential substrate of FBXL5, p150^{Glued} (Zhang et al., 2007), was not (Figure 3C). Such IRP accumulation was apparent even under iron-replete conditions. Consistent with this finding, the expression of proteins encoded by mRNA targets of IRPs was also deregulated: thus, the abundance of TfR1 (which mediates iron uptake) was increased, whereas that of ferritin (which mediates iron storage) was decreased likely as a result of IRP-mediated translational suppression (Figure 3C). However, the transcription of ferritin genes is also regulated by oxidative stress through an antioxidant-responsive element (ARE) in the 5′ region (MacKenzie et al., 2008). Indeed, the expression of ferritin was markedly increased at both mRNA (Figure S3E) and protein (Figure 3C) levels in *Fbxl5*$^{\Delta/\Delta}$ MEFs under the iron-replete condition, suggesting that transcriptional activation of ferritin genes by oxidative stress dominates the translational suppression mediated by constitutively active IRPs. Furthermore, the iron-dependent degradation of IRP2 was impaired in *Fbxl5*$^{\Delta/\Delta}$ MEFs (Figure 3D). Although the abundance of IRP1 in *Fbxl5*$^{\Delta/\Delta}$ MEFs was markedly increased compared with that in *Fbxl5*$^{+/+}$ MEFs, the half-life of this protein was long even in iron-replete *Fbxl5*$^{+/+}$ MEFs (Figure 3D), probably reflecting the fact that most IRP1s exist in the holo-IRP1 form, which is resistant to degradation in iron-replete cells (Recalcati et al., 2006). These results suggested that IRPs accumulate, resulting in an increase in total IRP activity, in FBXL5-deficient embryos and MEFs in a manner independent of iron conditions, leading to deregulation of IRP targets.

We next examined how such IRP hyperactivation affects cellular iron homeostasis. The levels of iron in isolated cytosolic and mitochondrial fractions (Figure S3F) were greater for *Fbxl5*$^{\Delta/\Delta}$ MEFs than for *Fbxl5*$^{+/+}$ MEFs (Figure 3E), suggesting that the accumulated IRPs promote iron loading in the cytosol and mitochondria, leading to oxidative stress, in the former cells. Thus, collectively, our observations suggested that the abundance and activity of IRPs are increased in a manner independent of iron conditions, leading to increased oxidative stress and embryonic death as a result of iron overload, in FBXL5-deficient mice.

Fbxl5$^{-/-}$*Irp2*$^{-/-}$ Mice Develop Normally

To test our hypothesis that IRP accumulation is responsible for the early embryonic death of *Fbxl5*$^{-/-}$ mice, we examined whether additional ablation of IRP2, which dominates control of iron homeostasis in vivo (Meyron-Holtz et al., 2004b), prevented the embryonic mortality of these animals. Whereas most *Fbxl5*$^{-/-}$ mice died in utero at E8.5, *Fbxl5*$^{-/-}$*Irp2*$^{-/-}$ mice developed normally and were fertile (Figures 4A and 4B). *Fbxl5*$^{-/-}$*Irp2*$^{-/-}$ mice were macroscopically indistinguishable from wild-type littermates and grew normally (Figure 4C).

Iron metabolism in *Fbxl5*$^{-/-}$*Irp2*$^{-/-}$ mice appeared almost identical to that in *Irp2*$^{-/-}$ mice, with some exceptions. *Irp2*$^{-/-}$ mice manifest mild microcytic anemia and an abnormal distribution of iron within the body, including iron accumulation in the liver and a reduced iron level in the spleen (Cooperman et al., 2005; Galy et al., 2005). The hematocrit and serum concentration of hemoglobin were significantly reduced in *Irp2*$^{-/-}$ mice in association with a normal erythrocyte count and a lower mean cell volume (Table 1). The hematologic parameters of *Fbxl5*$^{-/-}$*Irp2*$^{-/-}$ mice were indistinguishable from those of *Irp2*$^{-/-}$ mice. However, the serum iron concentration as well as transferrin saturation were increased in *Fbxl5*$^{-/-}$*Irp2*$^{-/-}$ mice, whereas these parameters did not differ between *Irp2*$^{-/-}$ and wild-type mice (Table 1). Although the precise mechanism underlying these paradoxical increases remains unknown, these results suggest that the microcytosis in *Fbxl5*$^{-/-}$*Irp2*$^{-/-}$ mice is not attributable to systemic iron deficiency. We also measured organ nonheme iron content and found that it was increased in the liver and decreased in the spleen of *Irp2*$^{-/-}$ mice, consistent with previous observations, whereas the liver iron content of *Fbxl5*$^{-/-}$*Irp2*$^{-/-}$ mice was significantly decreased compared with that of *Irp2*$^{-/-}$ mice (Figure 4D). Immunoblot analysis revealed that the abundance of ferroportin was not significantly changed in the liver of *Fbxl5*$^{-/-}$*Irp2*$^{-/-}$ mice (Figure S4A). The expression of the iron-storage protein ferritin was increased in the cerebrum, liver, and kidney of *Irp2*$^{-/-}$ mice (Figure 4E). However, the abundance of ferritin in the liver of *Fbxl5*$^{-/-}$*Irp2*$^{-/-}$ mice was decreased compared with that in *Irp2*$^{-/-}$ mice, mirroring the decrease in iron content. An electrophoretic mobility shift assay (EMSA) revealed that the IRE-binding activity of IRP1 in the liver of *Fbxl5*$^{-/-}$*Irp2*$^{-/-}$ mice was increased by ~20% compared with that in *Irp2*$^{-/-}$ mice (Figures S4B and S4C), which may account for the decreased ferritin level.

We generated *Fbxl5*$^{-/-}$*Irp2*$^{-/-}$ MEFs and analyzed the response of iron-related proteins in these cells to changes in iron availability. The abundance of IRP1 in *Fbxl5*$^{-/-}$*Irp2*$^{-/-}$ MEFs was increased compared with that in *Irp2*$^{-/-}$ MEFs, and this difference was associated with a slight increase in

(D) Nonheme iron content of the liver and spleen of *Fbxl5*$^{+/+}$*Irp2*$^{+/+}$ (n = 8), *Fbxl5*$^{+/+}$*Irp2*$^{-/-}$ (n = 8), *Fbxl5*$^{+/-}$*Irp2*$^{-/-}$ (n = 10), and *Fbxl5*$^{-/-}$*Irp2*$^{-/-}$ (n = 12) mice at 9–13 weeks of age. Data are mean ± SD. **p < 0.01 (Student's t test).

(E) Immunoblot analysis of extracts of the cerebrum, liver, and kidney of 11-week-old mice of the indicated genotypes with antibodies to ferritin and to Hsp90. Two animals were examined for each genotype.

(F) Primary cultured MEFs of the indicated genotypes were incubated for 16 hr in the absence or presence of FAC (100 μg/ml) or 100 μM DFO and were then subjected to immunoblot analysis with antibodies to the indicated proteins. The asterisk indicates a nonspecific band. See also Figure S4.

Table 1. Hematologic and Serum Iron Parameters of *Fbxl5*$^{-/-}$*Irp2*$^{-/-}$ Mice

Hematologic Parameters				
Parameter	*Fbxl5*$^{+/+}$*Irp2*$^{+/+}$ (n = 11)	*Fbxl5*$^{+/+}$*Irp2*$^{-/-}$ (n = 8)	*Fbxl5*$^{+/-}$*Irp2*$^{-/-}$ (n = 11)	*Fbxl5*$^{-/-}$*Irp2*$^{-/-}$ (n = 15)
RBC count (10^4/μl)	1000 ± 37.8	952 ± 60.1	998 ± 55.4	985 ± 40.0
MCV (fl)	52.4 ± 0.6	49.3 ± 0.7[a]	48.9 ± 1.1[a]	48.7 ± 1.0[a]
Hematocrit (%)	52.4 ± 2.2	47.0 ± 3.2[a]	48.6 ± 2.5[a]	48.0 ± 1.9[a]
Serum hemoglobin (g/dl)	15.9 ± 0.7	13.7 ± 0.9[a]	14.3 ± 0.7[a]	14.0 ± 0.5[a]
MCH (pg)	15.9 ± 0.2	14.4 ± 0.4[a]	14.3 ± 0.5[a]	14.2 ± 0.3[a]
MCHC (g/dl)	30.3 ± 0.3	29.3 ± 0.5[a]	29.3 ± 0.5[a]	29.2 ± 0.5[a]
Serum Iron Parameters				
Parameter	*Fbxl5*$^{+/+}$*Irp2*$^{+/+}$ (n = 6)	*Fbxl5*$^{+/+}$*Irp2*$^{-/-}$ (n = 6)	*Fbxl5*$^{+/-}$*Irp2*$^{-/-}$ (n = 6)	*Fbxl5*$^{-/-}$*Irp2*$^{-/-}$ (n = 8)
TIBC (μg/dl)	366 ± 26. 4	359 ± 44.4	398 ± 36.9	334 ± 36.6
Iron (μg/dl)	150 ± 33.1	152 ± 32.6	163 ± 30.7	209 ± 33.5[a]
Transferrin saturation (%)	41.4 ± 11.1	42.5 ± 8.8	41.0 ± 8.8	63.9 ± 15.2[a]

Data are mean ± SD for the indicated numbers of 9- to 13-week-old mice. Transferrin saturation was calculated from measured serum iron and TIBC. RBC, red blood cell; MCV, mean cell volume; MCH, mean corpuscular hemoglobin; MCHC, mean corpuscular hemoglobin concentration; TIBC, total iron-binding capacity.
[a] $p < 0.01$ versus *Fbxl5*$^{+/+}$*Irp2*$^{+/+}$ mice (Student's t test).

TfR1 expression under iron-replete conditions (Figure 4F). These observations suggested that IRP1 activity was slightly increased in *Fbxl5*$^{-/-}$*Irp2*$^{-/-}$ mice. Thus, we concluded that the increased activity of IRP1 in *Fbxl5*$^{-/-}$*Irp2*$^{-/-}$ mice attenuated the increased hepatic levels of iron and ferritin apparent in *Irp2*$^{-/-}$ mice.

Liver-Specific Ablation of *Fbxl5*

To study the function of FBXL5 in adult mouse tissues, we next examined the consequences of FBXL5 deficiency in the liver, which plays a central role in systemic iron homeostasis. To ablate *Fbxl5* in the liver, we crossed *Fbxl5*$^{F/F}$ mice with mice harboring a Cre transgene under the control of the promoter for the albumin gene (*Alb*-Cre mice). We confirmed that almost all floxed alleles were inactivated by Cre recombinase in the liver of *Alb*-Cre/*Fbxl5*$^{F/F}$ mice, as revealed by a corresponding decrease in the amount of FBXL5 mRNA (Figure S5A). *Alb*-Cre/*Fbxl5*$^{F/F}$ mice were viable, but the liver of these animals was lighter in color compared with that of their *Alb*-Cre/*Fbxl5*$^{F/+}$ littermates (Figure 5A). Histological analysis revealed that the nuclei of cells in the liver of *Alb*-Cre/*Fbxl5*$^{F/F}$ mice remained centrally located, whereas the corresponding cytoplasm was only weakly eosinophilic and contained numerous microvesicular vacuoles (Figures 5B and 5C). Lobular infiltration of inflammatory cells such as lymphocytes and neutrophils was also observed in the liver of *Alb*-Cre/*Fbxl5*$^{F/F}$ mice (Figure 5D), indicative of hepatic inflammation. However, serum chemistry parameters associated with liver damage did not differ between the mutant and control mice under normal fed conditions (Table S1), indicating that the hepatic inflammation in the mutant animals is mild. Oil red O staining revealed deposition of multiple small lipid droplets with an undisplaced nucleus in liver cells of the mutant mice (Figures 5E and 5F), a characteristic of liver damage associated with impaired mitochondrial function (Burt, 2001). Consistent with mitochondrial dysfunction, ATP levels of *Fbxl5*$^{\Delta/\Delta}$ MEFs under basal conditions were reduced compared with those of *Fbxl5*$^{+/+}$ MEFs, and this reduction was further enhanced under high-iron conditions (Figure S5B). Moreover, electron microscopy revealed mitochondriopathy associated with small lipid droplets in FBXL5-deficient hepatocytes; the mitochondria were swollen, with a hypodense matrix suggestive of mitochondrial injury (Figures 5G–5J).

We next examined iron metabolism in *Alb*-Cre/*Fbxl5*$^{F/F}$ mice. DAB-enhanced Perls and Turnbull staining revealed the accumulation of ferrous iron in hepatocytes of *Alb*-Cre/*Fbxl5*$^{F/F}$ mice (Figures 5K–5N). Immunoblot analysis showed that IRP2 also accumulated in the liver of these mice (Figure 5O). The abundance of IRP1 was also increased in the liver of *Alb*-Cre/*Fbxl5*$^{F/F}$ mice, but the extent of this change was much less pronounced than was that observed in *Fbxl5*$^{\Delta/\Delta}$ MEFs—probably because the iron-sulfur cluster of IRP1 is readily destabilized by exposure to oxygen in cultured cells, leading to conversion of holo-IRP1 to the IRE-binding, apo-IRP1 form. Given the predominance of holo-IRP1 and the conversion of only a small fraction of this form to apo-IRP1 in mouse tissues (Meyron-Holtz et al., 2004a), the amount of apo-IRP1 in the liver of *Alb*-Cre/*Fbxl5*$^{F/F}$ mice may be masked by the more abundant holo-IRP1, which is not degraded by FBXL5 (Salahudeen et al., 2009; Vashisht et al., 2009). The upregulation of IRP2 in the liver of *Alb*-Cre/*Fbxl5*$^{F/F}$ mice was also associated with increased TfR1 expression (Figure 5O) and iron accumulation specifically in the liver (Figure 5P). The abundance of ferritin in the liver of *Alb*-Cre/*Fbxl5*$^{F/F}$ mice was paradoxically also increased despite the accumulation of IRP2 (Figure 5O). The amount of mRNA for the L chain of ferritin in the liver was greater for *Alb*-Cre/*Fbxl5*$^{F/F}$ mice than for *Fbxl5*$^{F/F}$ littermates, and this increase was greatly enhanced under conditions of oxidative stress induced by feeding the animals a high-iron diet (Figure S5C). Given that iron loss induces degradation of ferritin by the proteasome (De Domenico et al., 2006), both transcriptional and posttranslational mechanisms may contribute to upregulation of ferritin that dominates over IRP-mediated translational suppression of ferritin mRNA in the liver of *Alb*-Cre/*Fbxl5*$^{F/F}$ mice.

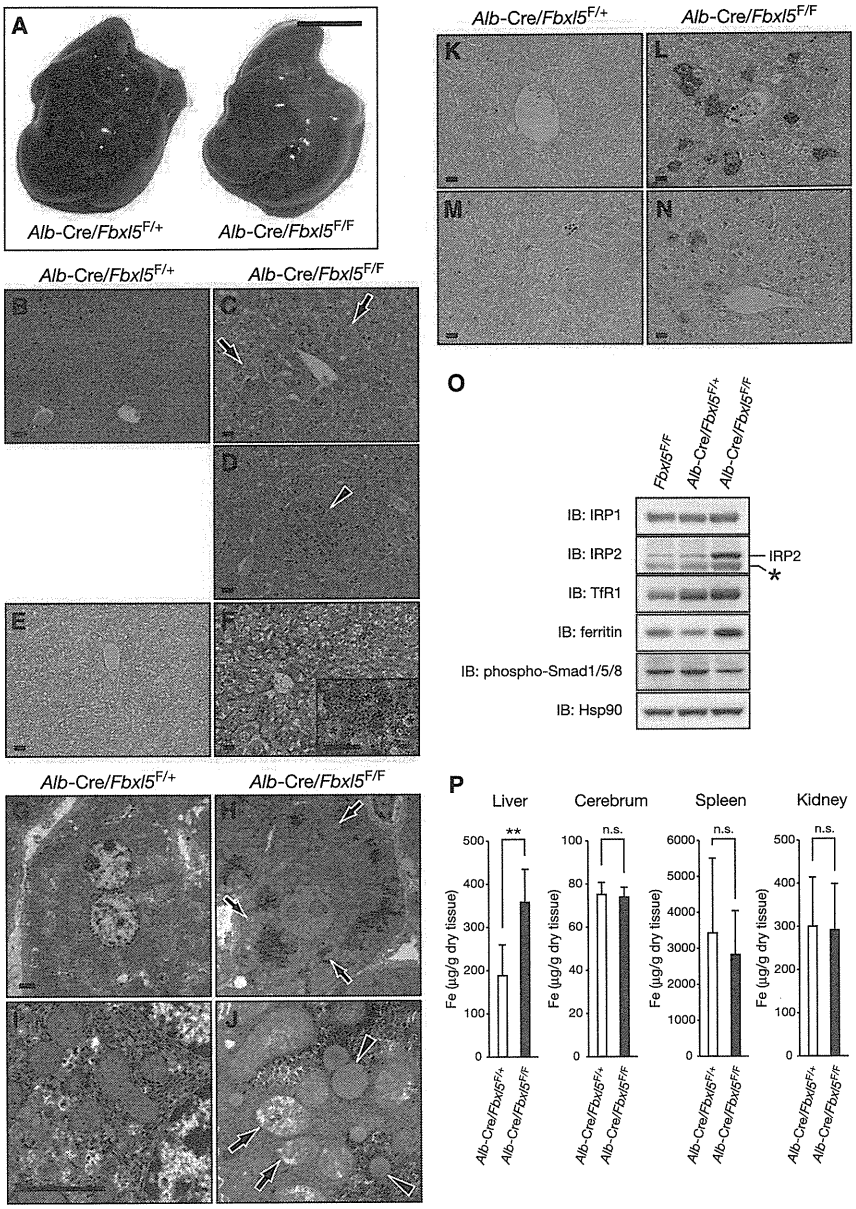

Figure 5. Hepatocyte-Specific Ablation of *Fbxl5* Results in Iron Accumulation and Steatohepatitis

(A) Gross appearance of the liver of *Alb*-Cre/*Fbxl5*$^{F/+}$ and *Alb*-Cre/*Fbxl5*$^{F/F}$ mouse littermates at 32 weeks of age. Scale bar, 10 mm.

(B–F) Histological analysis of the liver of 16- to 32-week-old *Alb*-Cre/*Fbxl5*$^{F/F}$ mice (C, D, and F) compared with that of control *Alb*-Cre/*Fbxl5*$^{F/+}$ littermates (B and E). (B–D) Hematoxylin and eosin staining. Arrows indicate numerous microvesicular vacuoles, and the arrowhead indicates lobular infiltration of inflammatory cells. (E and F) Oil red O staining. The inset in (F) shows a corresponding higher-magnification view. Asterisks indicate cell nuclei. Scale bars, 20 μm.

(G–J) Electron microscopy of the liver of 12-week-old *Alb*-Cre/*Fbxl5*$^{F/F}$ mice (H and J) compared with that of control *Alb*-Cre/*Fbxl5*$^{F/+}$ littermates (G and I). Arrows indicate numerous pale and swollen mitochondria, and the arrowheads indicate numerous lipid droplets. Scale bars, 2 μm.

(K–N) DAB-enhanced Perls staining (K and L) and DAB-enhanced Turnbull staining (M and N) of the liver of 16- to 32-week-old *Alb*-Cre/*Fbxl5*$^{F/F}$ mice (L and N) compared with that of control *Alb*-Cre/*Fbxl5*$^{F/+}$ littermates (K and M). Scale bars, 20 μm.

(O) Immunoblot analysis of liver extracts from 15-week-old mice of the indicated genotypes with antibodies to the indicated proteins. The asterisk indicates a nonspecific band.

(P) Nonheme iron content of the indicated organs of *Alb*-Cre/*Fbxl5*$^{F/+}$ (n = 4) and *Alb*-Cre/*Fbxl5*$^{F/F}$ (n = 8) mice at 16–32 weeks of age. Data are mean ± SD. n.s., not significant. **p < 0.01 (Student's t test). See also Figure S5 and Table S1.

Systemic Iron Overload in *Alb*-Cre/*Fbxl5*$^{F/F}$ Mice

We next asked how liver-specific deletion of *Fbxl5* affects systemic iron homeostasis. Serum iron levels (Figure 6A) as well as transferrin saturation (Figure 6B) were significantly increased in *Alb*-Cre/*Fbxl5*$^{F/F}$ mice, whereas hematologic parameters were not changed (Table S1). These results suggested that, inappropriately for their overall iron status, these mice might express low levels of hepcidin, the negative regulator of iron transport into plasma. The abundance of hepcidin mRNA in the liver was indeed significantly smaller for *Alb*-Cre/*Fbxl5*$^{F/F}$ mice than for *Fbxl5*$^{F/F}$ littermates (Figure 6C), and such a difference was also apparent when hepcidin gene expression was increased by feeding the animals a high-iron diet.

To elucidate the mechanism underlying the downregulation of hepcidin mRNA in the liver of *Alb*-Cre/*Fbxl5*$^{F/F}$ mice, we examined bone morphogenetic protein (BMP) signaling, which is the predominant regulator of hepcidin gene transcription (Hentze et al., 2010). Whereas the hepatic abundance of Hfe2 mRNA was unaffected (Figure S6A), that of BMP6 mRNA was smaller for *Alb*-Cre/*Fbxl5*$^{F/F}$ mice than for *Fbxl5*$^{F/F}$ littermates, and this difference was also apparent when *Bmp6* expression was increased by feeding the animals a high-iron diet (Figure S6B). We also examined receptor-activated Smad phosphorylation and found that the phosphorylation level of Smad1, Smad5, and Smad8 (Smad1/5/8) was decreased in the liver of *Alb*-Cre/*Fbxl5*$^{F/F}$ mice (Figure 5O). The amounts of mRNAs for suppressors of hepcidin gene transcription such as Smad6, Smad7, and transmembrane serine protease 6 (Tmprss6) were not increased in the liver of *Alb*-Cre/*Fbxl5*$^{F/F}$ mice, but rather were paradoxically decreased (Figure S6C). Increased iron did not activate Smad7 transcription in the liver of *Alb*-Cre/*Fbxl5*$^{F/F}$ mice, likely as a result of decreased BMP signaling (Kautz et al., 2008). Collectively, these findings indicated that BMP signaling in the liver of *Alb*-Cre/*Fbxl5*$^{F/F}$ mice is decreased as a result of the reduced expression of *Bmp6*, and they suggested that the decrease in *Bmp6* expression is likely responsible for downregulation of

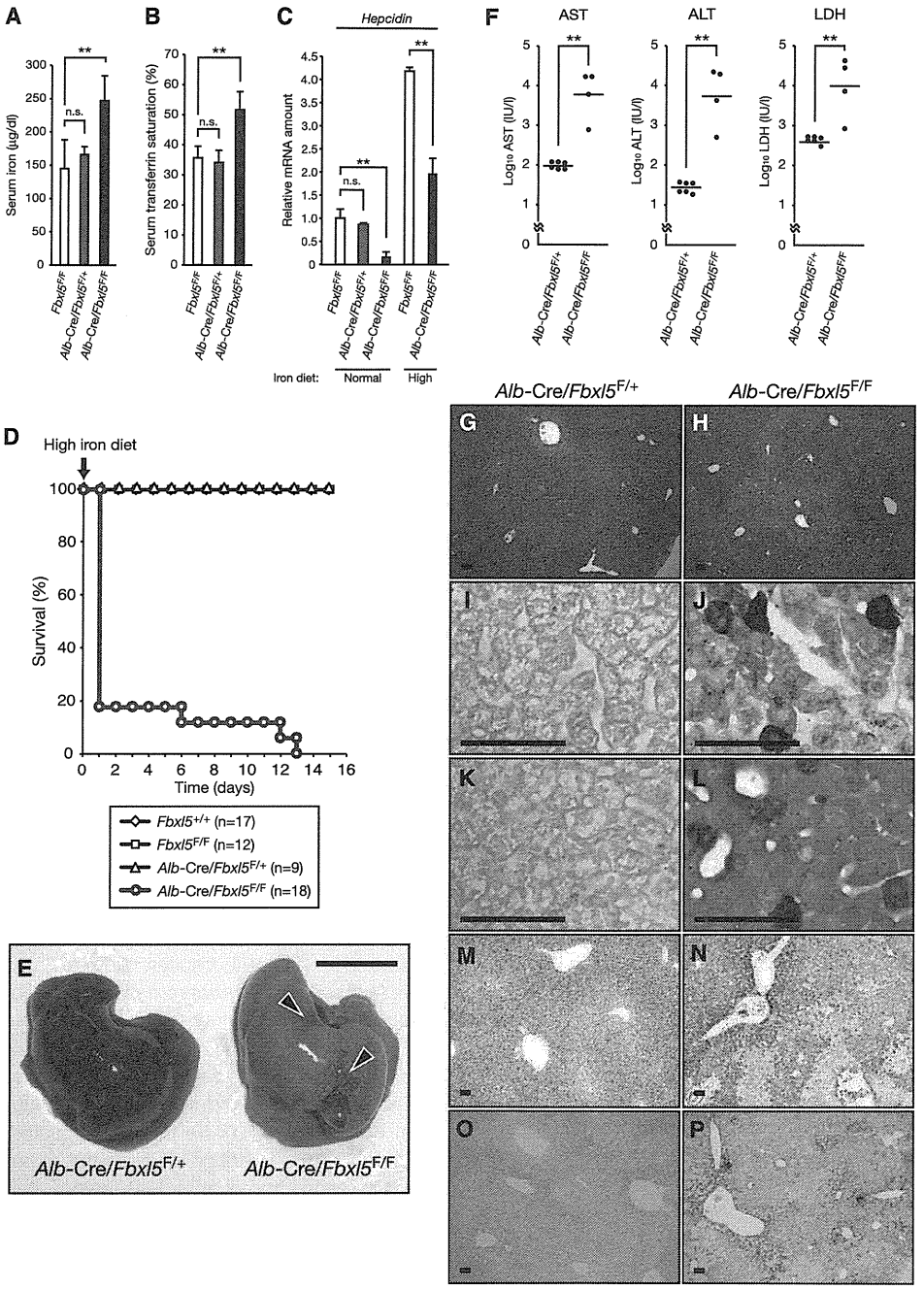

Figure 6. Fatal Liver Failure in *Alb*-Cre/*Fbxl5*$^{F/F}$ Mice Fed a High-Iron Diet

(A) Serum nonheme iron concentration in *Fbxl5*$^{F/F}$ (n = 4), *Alb*-Cre/*Fbxl5*$^{F/+}$ (n = 6), and *Alb*-Cre/*Fbxl5*$^{F/F}$ (n = 7) mice at 16–32 weeks of age. Data are mean ± SD. n.s., not significant. **p < 0.01 (Student's t test).

(B) Serum transferrin saturation in *Fbxl5*$^{F/F}$ (n = 3), *Alb*-Cre/*Fbxl5*$^{F/+}$ (n = 6), and *Alb*-Cre/*Fbxl5*$^{F/F}$ (n = 8) mice at 16–32 weeks of age. Transferrin saturation was calculated from measured total (TIBC) and unsaturated (UIBC) iron-binding capacities. Data are mean ± SD. **p < 0.01 (Student's t test).

(C) RT and real-time PCR analysis of hepcidin mRNA in the liver of 16-week-old mice of the indicated genotypes fed a normal diet or exposed to a high-iron diet for 1 day. Normalized data are expressed relative to the corresponding value for control mice (*Fbxl5*$^{F/F}$ mice fed a normal diet) and are mean ± SEM (n = 3 mice per group). **p < 0.01 (Student's t test).

(D) Kaplan-Meier survival curves for 6-week-old mice of the indicated genotypes after the start of a high-iron diet.

(E) Gross appearance of the liver of 6-week-old *Alb*-Cre/*Fbxl5*$^{F/+}$ and *Alb*-Cre/*Fbxl5*$^{F/F}$ littermates at 1 day after the start of a high-iron diet. Arrowheads indicate bleeding. Scale bar, 10 mm.

(F) Serum AST, ALT, and LDH activities in 6-week-old *Alb*-Cre/*Fbxl5*$^{F/+}$ (n = 6) and *Alb*-Cre/*Fbxl5*$^{F/F}$ (n = 4) mice at 1 day after the start of a high-iron diet. The results are plotted on a logarithmic ordinate, and horizontal lines indicate mean values. **p < 0.01 (Student's t test).

hepcidin in the liver of these mice. They further suggested that liver-specific ablation of FBXL5 results in systemic iron overload as a result of a reduced level of hepcidin secretion from the liver.

Fatal Liver Failure in *Alb*-Cre/*Fbxl5*$^{F/F}$ Mice Fed a High-Iron Diet

Given that hepcidin expression was downregulated in *Alb*-Cre/*Fbxl5*$^{F/F}$ mice, we next examined the effect of iron overload in these animals fed a high-iron diet. Whereas all control mice remained alive, most *Alb*-Cre/*Fbxl5*$^{F/F}$ mice died within 1 day, and the rest ate very little of the diet and lost weight, finally dying of starvation within 2 weeks (Figure 6D). Macroscopic examination of the *Alb*-Cre/*Fbxl5*$^{F/F}$ mice revealed prominent hemorrhage on the surface of the fatty liver (Figure 6E). Both prothrombin time (PT) and activated partial thromboplastin time (APTT) were significantly increased for *Alb*-Cre/*Fbxl5*$^{F/F}$ mice on the high-iron diet compared with those for *Fbxl5*$^{F/F}$ mice (Figure S6D), suggestive of a severe coagulopathy in the former animals. Serum levels of hepatic enzymes such as aspartate aminotransferase (AST), alanine aminotransferase (ALT), and lactate dehydrogenase (LDH) were also increased ~100-fold in these animals (Figure 6F), suggestive of an acute progressive destruction of hepatocytes. Changes in biliary tract enzymes were smaller than those in hepatic enzymes (Table S2). Histological analysis revealed massive cell death, predominantly in the area around portal veins, in the FBXL5-deficient liver (Figures 6G and 6H). DAB-enhanced Perls or Turnbull staining also revealed the accumulation of ferrous iron in the hepatocytes of *Alb*-Cre/*Fbxl5*$^{F/F}$ mice (Figures 6I–6L), whereas detection of 4-HNE-modified proteins revealed a marked increase in oxidative stress (Figures 6M and 6N). TUNEL-positive cells were also observed among hepatocytes of *Alb*-Cre/*Fbxl5*$^{F/F}$ mice (Figures 6O and 6P). Furthermore, oxidative stress and cell death in the liver were markedly attenuated by the addition of NAC to the drinking water of *Alb*-Cre/*Fbxl5*$^{F/F}$ mice fed the high-iron diet (Figure S6E). On the other hand, *Irp2*$^{-/-}$ mice did not die when fed a high-iron diet (n = 6, data not shown), probably because the accumulation of ferrous iron was much less pronounced than was that of ferric iron in these animals (Figure S6F). Given that the high-iron diet had little effect on the iron content of other organs of *Alb*-Cre/*Fbxl5*$^{F/F}$ mice (data not shown), these results indicated that *Alb*-Cre/*Fbxl5*$^{F/F}$ mice fed such a diet died of acute liver failure resulting from iron excess. Collectively, our observations implicate FBXL5 in the regulation of iron homeostasis both at the systemic level and in the liver.

DISCUSSION

We have shown that the loss of FBXL5 results in upregulation of IRP expression and activity, leading to fatal damage in embryos or the adult liver due to the excessive accumulation of ferrous iron. Our genetic evidence suggests that IRP2 is the major target of the SCF^{FBXL5} E3 ligase. Our findings further indicate that FBXL5 plays a central role in the maintenance of appropriate concentrations of intracellular iron and is essential for embryonic development as well as for normal postnatal liver physiology in mice.

Regulation of IRP activity is essential for cells to maintain an appropriate cytosolic LIP, thereby avoiding deleterious iron deficiency and preventing iron excess. FBXL5 recognizes both IRP1 and IRP2 and promotes their degradation in an iron-dependent manner. Our results now indicate that iron-dependent degradation of IRPs mediated by FBXL5 is pivotal for regulation of their activity as well as for iron homeostasis in mice. FBXL5 also senses intracellular iron through direct iron binding to its hemerythrin domain, resulting in FBXL5 stabilization (Salahudeen et al., 2009; Vashisht et al., 2009). Thus, FBXL5 acts as a sensor of the cytosolic LIP that negatively regulates this pool through degradation of IRPs.

Maintenance of the cytosolic LIP at an appropriate level is crucial, especially in cells exposed to iron overload. We found that *Fbxl5*$^{-/-}$ embryos die manifesting iron accumulation in the early placenta, and that *Fbxl5*$^{-/-}$ blastocysts do not survive under iron-replete conditions. These results suggest that FBXL5 is a key regulator that confers resistance to stress resulting from iron overload. During embryogenesis, FBXL5 plays an essential role in the early placental regions. Given that mice lacking the iron-exporting protein ferroportin, which transfers iron from the extraembryonic visceral endoderm (early placenta) into the embryo, die in utero (Donovan et al., 2005), these early placental regions appear to be essential for iron delivery to embryos, and they thereby need to endure stress attributable to iron overload. FBXL5 appears to protect these iron-transferring cells from damage due to excess iron.

FBXL5 also plays an essential role in normal postnatal liver physiology by preventing systemic iron overload. Hereditary hemochromatosis is a genetic disorder that leads to iron overload in the liver and other organs. Complications of this disease include liver cirrhosis, cancer, diabetes, and heart failure. To date, hereditary hemochromatosis has been attributed to defects in five genes, four of which give rise to recessive disorders (De Domenico et al., 2008). All recessive forms of the disease are associated with molecular defects in hepatocytes and are caused by inappropriately low levels of hepcidin expression. We have now shown that liver-specific ablation of FBXL5 results in downregulation of hepcidin expression and consequent systemic iron overload. Therefore, hepatic expression of FBXL5 might also be a determinant of iron overload disorders.

Iron overload status in FBXL5-deficient mice differs substantially from that in other mice showing simple systemic iron overload in terms of the valence of the accumulating iron (Fe^{2+} or Fe^{3+}). FBXL5-deficient mice manifest accumulation of dangerous ferrous iron (Fe^{2+}), whereas many other animal models such as mice deficient in Hfe1 (Zhou et al., 1998), Hfe2 (Niederkofler et al., 2005), or hepcidin (Lesbordes-Brion et al., 2006) exhibit accumulation of ferric iron (Fe^{3+}) in the liver as a result of defective hepcidin production. This point is key to understanding iron metabolism in *Alb*-Cre/*Fbxl5*$^{F/F}$ mice, which

(G–P) Histological analysis of the liver of 6-week-old *Alb*-Cre/*Fbxl5*$^{F/F}$ mice (H, J, L, N, and P) and control *Alb*-Cre/*Fbxl5*$^{F/+}$ littermates (G, I, K, M, and O) at 1 day after the start of a high-iron diet. Hematoxylin and eosin staining is shown in (G) and (H), DAB-enhanced Perls staining is shown in (I) and (J), DAB-enhanced Turnbull staining is shown in (K) and (L), immunohistochemical staining with antibodies to 4-HNE is shown in (M) and (N), and TUNEL staining is shown in (O) and (P). Scale bars, 100 μm. See also Figure S6 and Table S2.

fail to establish two barriers that protect against dietary iron overload: the hepcidin-dependent intestinal barrier against iron hyperabsorption, and the FBXL5-dependent intracellular barrier against an inappropriate increase in the LIP. The aforementioned other mutant mice retain the latter barrier, which minimizes an inappropriate increase in the LIP. Thus, hepatic FBXL5 deficiency gives rise to iron poisoning that is more severe than that that results from simple systemic iron overload due to dietary iron excess.

Hepatic iron overload is a pathophysiologic feature of nonalcoholic steatohepatitis (NASH), chronic liver disease associated with hepatitis C virus infection, and hepatocellular carcinoma (Sorrentino et al., 2009). Excess ferrous iron generates hydroxyl radicals that give rise to chronic inflammation, DNA damage, genetic instability, and tumorigenesis as a result of oxidative stress. Although iron accumulation itself may not initiate chronic liver disease, it has a detrimental effect on disease progression. We have now shown that liver-specific ablation of FBXL5 results in an increased hepatic iron content, systemic iron overload, and acute fatal liver failure in the presence of dietary iron overload. *Alb*-Cre/*Fbxl5*$^{F/F}$ mice develop steatosis and inflammation of the liver, reminiscent of human NASH, likely as a result of mitochondrial damage. Increased serum iron levels might worsen the liver damage in *Alb*-Cre/*Fbxl5*$^{F/F}$ mice. Thus, we speculate that a reduced level of FBXL5 expression in the human liver might give rise to a vicious cycle of liver damage and contribute to the progression of chronic inflammation and liver cancer.

EXPERIMENTAL PROCEDURES

Generation of *Fbxl5*$^{-/-}$ and *Fbxl5*$^{-/-}$*Irp2*$^{-/-}$ Mice

The targeting vector for *Fbxl5* was constructed by replacement of a 3.1 kb fragment of genomic DNA containing exons 4 and 5 of *Fbxl5* with IRES-*lacZ* and PGK-*neo*-poly(A)-loxP cassettes. A diphtheria toxin A (DT-A) cassette was ligated at the 3′ end of the targeting construct. Maintenance, transfection, and selection of mouse ESCs were performed as described previously (Nakayama et al., 1996). Mutant ESCs were microinjected into C57BL/6 blastocysts, and resulting chimeras were mated with C57BL/6 mice. Heterozygous offspring were intercrossed to produce homozygous mutant animals and their littermate controls. For assessment of their growth capability, preimplantation embryos were cultured as described previously (Nishiyama et al., 2009). All mice in this study were backcrossed to the C57BL/6 background for more than six generations. *Fbxl5*$^{+/-}$ mice were also crossed with *Irp2*$^{-/-}$ mice (LaVaute et al., 2001) obtained from Mutant Mouse Regional Resource Centers. *Fbxl5*$^{+/-}$*Irp2*$^{+/-}$ offspring were intercrossed to produce *Fbxl5*$^{-/-}$*Irp2*$^{-/-}$ animals and their littermate controls.

Generation of Conditional Knockout Mice

The 5′ and 3′ regions of homology in the targeting vector for *Fbxl5* consisted of a 1.2 kb fragment of intron 3 and an 8.5 kb fragment spanning introns 3 and 7, respectively. The neomycin-resistance gene (*neo*) flanked by loxP sites was isolated from the plasmid pL2-Neo(2) (kindly provided by D.R. Littman) (Gu et al., 1993) and inserted upstream of exon 4 of *Fbxl5*. A loxP site was also inserted downstream of exon 5. ES clones that had undergone homologous recombination were transfected with pMC-Cre (kindly provided by D.R. Littman) to excise the loxP-*neo* cassette. Mutant ESCs were then microinjected into C57BL/6 blastocysts, and the resulting chimeras were mated with C57BL/6 mice. Heterozygous offspring were intercrossed to produce homozygous mutant animals (*Fbxl5*$^{F/F}$). *Fbxl5*$^{F/F}$ mice were then crossed with *Alb*-Cre transgenic mice (Postic and Magnuson, 2000) obtained from The Jackson Laboratory to produce *Alb*-Cre/*Fbxl5*$^{F/F}$ mice. A high-iron diet was formulated by supplementation of CA-1 (containing 0.03% [w/w] ferric citrate; CLEA Japan) with 2% (w/w) ferric citrate. All animals were maintained under the specific pathogen-free (SPF) condition, and all experiments were approved by the animal ethics committee of Kyushu University.

Iron Histochemistry

Mice (pregnant for analysis of embryos) were anesthetized by intravenous injection of pentobarbital sodium (648 mg/kg) and were then perfused consecutively with 50 mM hydrogen sulfide in deionized water and with 4% paraformaldehyde in phosphate-buffered saline. Iron was detected in cryostat sections by enhanced Perls or Turnbull staining. Tissue sections were washed with deionized water, incubated for 30 min with Perls reagent (5% potassium ferrocyanide, 5% HCl) or with Turnbull reagent (5% potassium ferricyanide, 5% HCl), and then washed again in deionized water before incubation first for 15 min with unactivated DAB (0.05% DAB in deionized water) and then for 10 min with activated DAB (0.05% DAB, 1% H_2O_2). Tissue sections of control and mutant mice were stained at the same time to allow monitoring and detection of nonspecific staining.

Whole-Mount In Situ Hybridization

Whole-mount in situ hybridization was performed as described previously (Nishiyama et al., 2009). An FBXL5 antisense riboprobe corresponding to nucleotides 396–765 of the cDNA was synthesized with the use of a DIG RNA labeling kit (Roche).

RT and Real-Time PCR Analysis

RT and real-time PCR analysis was performed as described previously (Onoyama et al., 2011). Purification of mRNA from embryos was performed with the use of a TurboCapture mRNA Kit (QIAGEN). The sequences of the PCR primers (forward and reverse, respectively) were: 5′-GGTGATCCATACA CACCTGGCTT-3′ and 5′-TGATGACTGAGATGGCGGAA-3′ for TfR1; 5′-CC TATCTCCATCAACAGAT-3′ and 5′-TGCAACAGATACCACACTG-3′ for hepcidin 1 (Hamp1); and 5′-GGACCCGAGAAGACCTCCTT-3′ and 5′-GCACATCAC TCAGAATTTCAATGG-3′ for ARBP (attachment region-binding protein). Reactions for ARBP mRNA were performed concurrently on the same plate as those for the test mRNAs, and results were normalized by the corresponding amount of ARBP mRNA.

Immunoblot Analysis

Immunoblot analysis was performed as previously described (Onoyama et al., 2011) with antibodies to IRP1 (sc-14216; Santa Cruz Biotechnology), to p150^{Glued} (610473; BD Transduction Laboratories), to phosphorylated Smad1(Ser$^{463/465}$)/Smad5(Ser$^{463/465}$)/Smad8(Ser$^{426/428}$) (9511; Cell Signaling Technology), to ferritin (F6136; Sigma-Aldrich), to TfR1 (13-6800; Invitrogen), to Hsp90 (610419; BD Biosciences), and to IRP2 (generated by K. Iwai, Osaka University).

Statistical Analysis

Quantitative data are presented as mean ± SEM or ± SD as indicated and were compared between groups with the two-tailed Student's t test as performed with Microsoft Excel software. A p value of <0.05 was considered statistically significant.

SUPPLEMENTAL INFORMATION

Supplemental Information includes Supplemental Experimental Procedures, Supplemental References, six figures, and two tables and can be found with this article online at doi:10.1016/j.cmet.2011.07.011.

ACKNOWLEDGMENTS

We thank T. Rouault for *Irp2*$^{-/-}$ mice; D.R. Littman for pL2-Neo(2) and pMC-Cre; T. Kitamura for pMX-puro; M. Tanaka, Y. Yamada, K. Takeda, M. Sasaki, R. Ugawa, M. Oda, E. Koba, and N. Kinoshita for technical assistance; and D. Kang, S. Toyokuni, S. Sakata, and T. Asano for discussion.

Received: March 30, 2011
Revised: June 23, 2011
Accepted: July 19, 2011
Published: September 6, 2011

REFERENCES

Andrews, N.C., and Schmidt, P.J. (2007). Iron homeostasis. Annu. Rev. Physiol. *69*, 69–85.

Burt, A.D. (2001). Steatosis and steatohepatitis. Curr. Diagn. Pathol. *7*, 141–147.

Cooperman, S.S., Meyron-Holtz, E.G., Olivierre-Wilson, H., Ghosh, M.C., McConnell, J.P., and Rouault, T.A. (2005). Microcytic anemia, erythropoietic protoporphyria, and neurodegeneration in mice with targeted deletion of iron-regulatory protein 2. Blood *106*, 1084–1091.

Cross, J.C., Werb, Z., and Fisher, S.J. (1994). Implantation and the placenta: key pieces of the development puzzle. Science *266*, 1508–1518.

De Domenico, I., McVey Ward, D., and Kaplan, J. (2008). Regulation of iron acquisition and storage: consequences for iron-linked disorders. Nat. Rev. Mol. Cell Biol. *9*, 72–81.

De Domenico, I., Vaughn, M.B., Li, L., Bagley, D., Musci, G., Ward, D.M., and Kaplan, J. (2006). Ferroportin-mediated mobilization of ferritin iron precedes ferritin degradation by the proteasome. EMBO J. *25*, 5396–5404.

Donovan, A., Lima, C.A., Pinkus, J.L., Pinkus, G.S., Zon, L.I., Robine, S., and Andrews, N.C. (2005). The iron exporter ferroportin/Slc40a1 is essential for iron homeostasis. Cell Metab. *1*, 191–200.

Galy, B., Ferring, D., Minana, B., Bell, O., Janser, H.G., Muckenthaler, M., Schümann, K., and Hentze, M.W. (2005). Altered body iron distribution and microcytosis in mice deficient in iron regulatory protein 2 (IRP2). Blood *106*, 2580–2589.

Gu, H., Zou, Y.R., and Rajewsky, K. (1993). Independent control of immunoglobulin switch recombination at individual switch regions evidenced through Cre-loxP-mediated gene targeting. Cell *73*, 1155–1164.

Hentze, M.W., Muckenthaler, M.U., Galy, B., and Camaschella, C. (2010). Two to tango: regulation of Mammalian iron metabolism. Cell *142*, 24–38.

Jin, J., Cardozo, T., Lovering, R.C., Elledge, S.J., Pagano, M., and Harper, J.W. (2004). Systematic analysis and nomenclature of mammalian F-box proteins. Genes Dev. *18*, 2573–2580.

Kautz, L., Meynard, D., Monnier, A., Darnaud, V., Bouvet, R., Wang, R.H., Deng, C., Vaulont, S., Mosser, J., Coppin, H., and Roth, M.P. (2008). Iron regulates phosphorylation of Smad1/5/8 and gene expression of Bmp6, Smad7, Id1, and Atoh8 in the mouse liver. Blood *112*, 1503–1509.

LaVaute, T., Smith, S., Cooperman, S., Iwai, K., Land, W., Meyron-Holtz, E., Drake, S.K., Miller, G., Abu-Asab, M., Tsokos, M., et al. (2001). Targeted deletion of the gene encoding iron regulatory protein-2 causes misregulation of iron metabolism and neurodegenerative disease in mice. Nat. Genet. *27*, 209–214.

Lesbordes-Brion, J.C., Viatte, L., Bennoun, M., Lou, D.Q., Ramey, G., Houbron, C., Hamard, G., Kahn, A., and Vaulont, S. (2006). Targeted disruption of the hepcidin 1 gene results in severe hemochromatosis. Blood *108*, 1402–1405.

MacKenzie, E.L., Iwasaki, K., and Tsuji, Y. (2008). Intracellular iron transport and storage: from molecular mechanisms to health implications. Antioxid. Redox Signal. *10*, 997–1030.

Meguro, R., Asano, Y., Iwatsuki, H., and Shoumura, K. (2003). Perfusion-Perls and -Turnbull methods supplemented by DAB intensification for nonheme iron histochemistry: demonstration of the superior sensitivity of the methods in the liver, spleen, and stomach of the rat. Histochem. Cell Biol. *120*, 73–82.

Meyron-Holtz, E.G., Ghosh, M.C., and Rouault, T.A. (2004a). Mammalian tissue oxygen levels modulate iron-regulatory protein activities in vivo. Science *306*, 2087–2090.

Meyron-Holtz, E.G., Ghosh, M.C., Iwai, K., LaVaute, T., Brazzolotto, X., Berger, U.V., Land, W., Ollivierre-Wilson, H., Grinberg, A., Love, P., and Rouault, T.A. (2004b). Genetic ablations of iron regulatory proteins 1 and 2 reveal why iron regulatory protein 2 dominates iron homeostasis. EMBO J. *23*, 386–395.

Muckenthaler, M.U., Galy, B., and Hentze, M.W. (2008). Systemic iron homeostasis and the iron-responsive element/iron-regulatory protein (IRE/IRP) regulatory network. Annu. Rev. Nutr. *28*, 197–213.

Nakayama, K., Ishida, N., Shirane, M., Inomata, A., Inoue, T., Shishido, N., Horii, I., Loh, D.Y., and Nakayama, K.I. (1996). Mice lacking p27(^{Kip1}) display increased body size, multiple organ hyperplasia, retinal dysplasia, and pituitary tumors. Cell *85*, 707–720.

Nakayama, K.I., and Nakayama, K. (2006). Ubiquitin ligases: cell-cycle control and cancer. Nat. Rev. Cancer *6*, 369–381.

Nemeth, E., Tuttle, M.S., Powelson, J., Vaughn, M.B., Donovan, A., Ward, D.M., Ganz, T., and Kaplan, J. (2004). Hepcidin regulates cellular iron efflux by binding to ferroportin and inducing its internalization. Science *306*, 2090–2093.

Niederkofler, V., Salie, R., and Arber, S. (2005). Hemojuvelin is essential for dietary iron sensing, and its mutation leads to severe iron overload. J. Clin. Invest. *115*, 2180–2186.

Nishiyama, M., Oshikawa, K., Tsukada, Y., Nakagawa, T., Iemura, S., Natsume, T., Fan, Y., Kikuchi, A., Skoultchi, A.I., and Nakayama, K.I. (2009). CHD8 suppresses p53-mediated apoptosis through histone H1 recruitment during early embryogenesis. Nat. Cell Biol. *11*, 172–182.

Onoyama, I., Suzuki, A., Matsumoto, A., Tomita, K., Katagiri, H., Oike, Y., Nakayama, K., and Nakayama, K.I. (2011). Fbxw7 regulates lipid metabolism and cell fate decisions in the mouse liver. J. Clin. Invest. *121*, 342–354.

Postic, C., and Magnuson, M.A. (2000). DNA excision in liver by an albumin-Cre transgene occurs progressively with age. Genesis *26*, 149–150.

Recalcati, S., Alberghini, A., Campanella, A., Gianelli, U., De Camilli, E., Conte, D., and Cairo, G. (2006). Iron regulatory proteins 1 and 2 in human monocytes, macrophages and duodenum: expression and regulation in hereditary hemochromatosis and iron deficiency. Haematologica *91*, 303–310.

Rouault, T.A., and Tong, W.H. (2005). Iron-sulphur cluster biogenesis and mitochondrial iron homeostasis. Nat. Rev. Mol. Cell Biol. *6*, 345–351.

Salahudeen, A.A., Thompson, J.W., Ruiz, J.C., Ma, H.W., Kinch, L.N., Li, Q., Grishin, N.V., and Bruick, R.K. (2009). An E3 ligase possessing an iron-responsive hemerythrin domain is a regulator of iron homeostasis. Science *326*, 722–726.

Sorrentino, P., D'Angelo, S., Ferbo, U., Micheli, P., Bracigliano, A., and Vecchione, R. (2009). Liver iron excess in patients with hepatocellular carcinoma developed on non-alcoholic steato-hepatitis. J. Hepatol. *50*, 351–357.

Vashisht, A.A., Zumbrennen, K.B., Huang, X., Powers, D.N., Durazo, A., Sun, D., Bhaskaran, N., Persson, A., Uhlen, M., Sangfelt, O., et al. (2009). Control of iron homeostasis by an iron-regulated ubiquitin ligase. Science *326*, 718–721.

Wang, J., and Pantopoulos, K. (2011). Regulation of cellular iron metabolism. Biochem. J. *434*, 365–381.

Zhang, N., Liu, J., Ding, X., Aikhionbare, F., Jin, C., and Yao, X. (2007). FBXL5 interacts with p150^{Glued} and regulates its ubiquitination. Biochem. Biophys. Res. Commun. *359*, 34–39.

Zhou, X.Y., Tomatsu, S., Fleming, R.E., Parkkila, S., Waheed, A., Jiang, J., Fei, Y., Brunt, E.M., Ruddy, D.A., Prass, C.E., et al. (1998). HFE gene knockout produces mouse model of hereditary hemochromatosis. Proc. Natl. Acad. Sci. USA *95*, 2492–2497.

Research article

Fbxw7 regulates lipid metabolism and cell fate decisions in the mouse liver

Ichiro Onoyama,[1,2] Atsushi Suzuki,[3,4] Akinobu Matsumoto,[1,2] Kengo Tomita,[5] Hideki Katagiri,[6] Yuichi Oike,[4,7] Keiko Nakayama,[2,8] and Keiichi I. Nakayama[1,2]

[1]Department of Molecular and Cellular Biology, Medical Institute of Bioregulation, Kyushu University, Higashi-ku, Fukuoka, Fukuoka, Japan. [2]CREST, Japan Science and Technology Agency, Kawaguchi, Saitama, Japan. [3]Division of Organogenesis and Regeneration, Medical Institute of Bioregulation, Kyushu University, Higashi-ku, Fukuoka, Fukuoka, Japan. [4]PRESTO, Japan Science and Technology Agency, Kawaguchi, Saitama, Japan. [5]Division of Gastroenterology and Hepatology, Department of Internal Medicine, National Defense Medical College, Tokorozawa, Saitama, Japan. [6]Division of Advanced Therapeutics for Metabolic Diseases, Center for Translational and Advanced Animal Research, Tohoku University Graduate School of Medicine, Sendai, Japan. [7]Department of Molecular Genetics, Graduate School of Medical Sciences, Kumamoto University, Kumamoto, Japan. [8]Division of Developmental Genetics, Center for Translational and Advanced Animal Research, Tohoku University Graduate School of Medicine, Sendai, Japan.

E3 ubiquitin ligase complexes of the SCF type consist of ring-box 1 (Rbx1), cullin 1 (Cul1), S-phase kinase-associated protein 1 (Skp1), and a member of the F-box family of proteins. The identity of the F-box protein determines the substrate specificity of the complex. The F-box family member F-box– and WD repeat domain–containing 7 (Fbxw7; also known as Fbw7, SEL-10, hCdc4, and hAgo) targets for degradation proteins with wide-ranging functions, and uncovering its in vivo role has been difficult, because *Fbxw7*$^{-/-}$ embryos die in utero. Using two different Cre-loxP systems (*Mx1*-Cre and *Alb*-Cre), we generated mice with liver-specific null mutations of *Fbxw7*. Hepatic ablation of *Fbxw7* resulted in hepatomegaly and steatohepatitis, with massive deposition of triglyceride, a phenotype similar to that observed in humans with nonalcoholic steatohepatitis. Both cell proliferation and the abundance of Fbxw7 substrates were increased in the Fbxw7-deficient liver. Long-term Fbxw7 deficiency resulted in marked proliferation of the biliary system and the development of hamartomas. Fbxw7 deficiency also skewed the differentiation of liver stem cells toward the cholangiocyte lineage rather than the hepatocyte lineage in vitro. This bias was corrected by additional loss of the Notch cofactor RBP-J, suggesting that Notch accumulation triggered the abnormal proliferation of the biliary system. Together, our results suggest that Fbxw7 plays key roles, regulating lipogenesis and cell proliferation and differentiation in the liver.

Introduction

The abundance of cellular proteins is regulated in a coordinated manner at the levels of their synthesis and degradation. In particular, intracellular proteolysis is thought to be subject to highly specific regulation. The ubiquitin-proteasome system is responsible for such specific degradation of proteins, with ubiquitylation playing the regulatory role in this process. Ubiquitylation of target proteins is mediated by the sequential action of 3 enzymes: a ubiquitin-activating enzyme (E1), a ubiquitin-conjugating enzyme (E2), and a ubiquitin ligase (E3). The ubiquitylated substrates are then selectively recognized and degraded by the 26S proteasome (1). Uncontrolled proteolysis is implicated in dysregulation of cell proliferation and aberrant cell differentiation and is thought to underlie many human malignancies (2).

F-box proteins determine the substrate specificity of the SCF-type E3 complex, which consists of the RING-finger protein ring-box 1 (Rbx1; also known as Roc1 and Hrt1), the scaffold protein cullin 1 (Cul1), and the adaptor protein S-phase kinase-associated protein 1 (Skp1) in addition to an F-box protein (2–4). F-box– and WD repeat domain–containing 7 (Fbxw7; also known as Fbw7, SEL-10, hCdc4, and hAgo) is a member of the F-box protein family that was initially identified as a negative regulator of LIN-12–mediated (Notch-mediated) signaling in *Caenorhabditis elegans* by genetic analysis (5, 6). Fbxw7 also interacts with Notch family proteins and promotes their ubiquitin-dependent turnover in mammalian cells (5, 7, 8). Furthermore, it targets for degradation various mammalian proteins that control cell cycle progression (2, 4), including cyclin E (9–11), c-Myc (12, 13), and c-Jun (14, 15), as well as other proteins that do not contribute directly to cell cycle control, such as SREBPs (16–18), mammalian target of rapamycin (mTOR) (19), and PPAR-γ coactivator-1α (PGC-1α) (20).

Given its ability to promote degradation of cyclin E, c-Myc, c-Jun, and Notch, all of which are products of proto-oncogenes, Fbxw7 was expected to function as an oncosuppressor protein. Indeed, mutations in the *Fbxw7* gene have been detected in many types of human malignancy, including cholangiocarcinoma and T cell acute lymphoblastic leukemia as well as pancreatic, gastric, colorectal, prostate, and endometrial cancer (21–31). The study of Fbxw7 is thus important not only from the point of view of basic biology but also from the medical standpoint.

To analyze the functions of Fbxw7 in vivo, we and others have generated Fbxw7-deficient mice. However, *Fbxw7*$^{-/-}$ embryos were found to die in utero at E10.5, manifesting marked abnormalities in vascular development as a result of dysregulation of Notch signaling (32, 33). To avoid this early embryonic mortality, we have established mice in which *Fbxw7* is conditionally disrupted in T cells (34) or in hematopoietic stem cells (35), and we have also examined the effects of *Fbxw7* ablation in mouse embryonic fibroblasts (36). The loss of Fbxw7 in immature T cells results in the failure of these cells to exit the cell cycle, leading to thymic hyperplasia and the subsequent development of lymphoma. Among known targets of Fbxw7, only c-Myc and Notch accumulated in the Fbxw7-deficient thymocytes, and c-Myc accumulation was found

Conflict of interest: The authors have declared that no conflict of interest exists.
Citation for this article: *J Clin Invest.* 2010;121(1):342–354. doi:10.1172/JCI40725.

to be primarily responsible for the hyperproliferation phenotype. In contrast to that in immature T cells, the accumulation of c-Myc apparent in Fbxw7-null mature T cells induced expression of p53, which in turn led to cell cycle arrest and apoptosis. Furthermore, we found that Fbxw7 contributes to the long-term maintenance of hematopoietic stem cells. Most of the phenotypes of Fbxw7 deficiency in these conditional mouse mutants are related to cell proliferation or death and appear to be attributable to deregulation of c-Myc and Notch. Although Fbxw7 targets many substrates that do not participate directly in cell cycle control for degradation, the physiological roles of Fbxw7-mediated degradation of such targets have been largely unclear.

We have now examined the consequences of Fbxw7 deficiency in the liver. Unexpectedly, the major phenotypes associated with such deficiency were abnormalities in lipid metabolism and cell differentiation, which differ markedly from those in hematopoietic cell lineages and fibroblasts, in which Fbxw7 contributes primarily to the control of cell proliferation and apoptosis. We thus propose that Fbxw7 targets different groups of proteins for ubiquitin-dependent degradation and thereby contributes to distinct biological functions in a tissue-specific manner.

Results

Conditional inactivation of Fbxw7 in the liver by 2 Cre-loxP systems. We generated mice harboring floxed *Fbxw7* alleles (referred to herein as *Fbxw7*$^{F/F}$ mice) in which exon 5 (which encodes the F-box domain) is flanked by loxP sites (34). To ablate *Fbxw7* in the liver, we crossed these *Fbxw7*$^{F/F}$ mice with mice harboring a Cre transgene under the control of the promoter for the myxovirus resistance 1 (*Mx1*) or albumin (*Alb*) genes (*Mx1*-Cre or *Alb*-Cre mice). We confirmed that almost all floxed alleles were inactivated by Cre recombinase in the livers of *Alb*-Cre/*Fbxw7*$^{F/F}$ mice as well as in those of *Mx1*-Cre/*Fbxw7*$^{F/F}$ mice at 3 weeks after the last of 3 i.p. injections of poly(I)-poly(C) (pIpC) to activate the *Mx1* gene promoter (Figure 1A). For subsequent experiments, we examined the effects of short- or long-term Fbxw7 deficiency in *Mx1*-Cre/*Fbxw7*$^{F/F}$ mice and those of long-term a priori deficiency in *Alb*-Cre/*Fbxw7*$^{F/F}$ mice.

Massive lipid deposition and nonalcoholic steatohepatitis–like lesions in the Fbxw7-deficient liver. *Mx1*-Cre/*Fbxw7*$^{F/F}$ mice at 8 weeks of age were subjected to i.p. injection of pIpC every other day for 3 days to activate the *Mx1* gene promoter. At 3 weeks after the last injection of pIpC, the livers of these mice were enlarged and lighter in color compared with those of control animals (Figure 1B). The liver-to-body weight ratio of these *Mx1*-Cre/*Fbxw7*$^{F/F}$ mice was increased by approximately 30% relative to that of control mice (Figure 1C). Histological examination revealed that the nuclei of cells in the enlarged liver remained centrally located, whereas the corresponding cytoplasm was only weakly eosinophilic and contained numerous microvesicular vacuoles (Figure 1, D and E). Staining with Oil red O (Figure 1, F–I) also revealed massive lipid deposition, predominantly in the area around central veins (Figure 1G). Similar lipid deposition was also observed in the livers of *Alb*-Cre/*Fbxw7*$^{F/F}$ mice at as early as 12 weeks of age (Figure 1, J and K). The mechanism underlying such an uneven localization of lipid deposition is unclear and awaits further investigation.

Lobular infiltration of inflammatory cells such as lymphocytes and neutrophils (Figure 1, L and M; arrowhead), as well as the presence of many ballooned hepatocytes (occasionally containing Mallory body–like eosinophilic inclusions) (Figure 1, N and O; arrow), were observed in the livers of older mutant mice at approximately 50 weeks of age. Sinusoidal fibrogenic changes in the liver as revealed by Masson's trichrome staining were also evident (Figure 1, P and Q), and serum levels of aspartate aminotransferase (AST) and alanine aminotransferase (ALT) were significantly increased (Figure 1R) in *Alb*-Cre/*Fbxw7*$^{F/F}$ mice at 50 weeks of age. The serum level of bilirubin tended to be higher in the mutant animals than in age-matched controls, suggestive of the destruction of liver tissue in the mutant mice, although this difference was not statistically significant (Supplemental Figure 1; supplemental material available online with this article; doi:10.1172/JCI40725DS1). The onset of inflammatory changes occurred later than that of steatosis, but feeding *Mx1*-Cre/*Fbxw7*$^{F/F}$ mice a methionine- and choline-deficient (MCD) diet resulted in acceleration of inflammation (Figure 2A). The extents of steatosis and hepatitis were less pronounced in *Alb*-Cre/*Fbxw7*$^{F/F}$ mice than in *Mx1*-Cre/*Fbxw7*$^{F/F}$ mice subjected to acute ablation of Fbxw7, probably as a result of compensatory mechanisms operative during development in the former animals. However, massive steatosis and inflammation were also apparent in *Alb*-Cre/*Fbxw7*$^{F/F}$ mice fed the MCD diet, whereas control animals did not show such marked changes (Figure 2B). These results suggested that *Alb*-Cre/*Fbxw7*$^{F/F}$ mice are also more sensitive to steatohepatitis than are controls. The histological findings in both types of Fbxw7-deficient mice are highly similar to those associated with nonalcoholic steatohepatitis (NASH) in humans (37).

Expression of adipogenic and lipogenic genes in the Fbxw7-deficient liver. We next determined lipid concentrations in liver extracts. Triglyceride levels were significantly increased in the livers of *Mx1*-Cre/*Fbxw7*$^{F/F}$ mice compared with those in control animals at 3 weeks after the final pIpC injection, whereas the concentration of total cholesterol was not affected in the mutant livers (Figure 3A). Given that triglyceride synthesis is regulated predominantly by transcriptional activators, such as SREBPs, carbohydrate response element–binding protein (ChREBP), and PPAR-γ, we examined the expression of these proteins and their downstream targets in the liver. Immunoblot analysis revealed that the abundance of nuclear SREBP1, which is the major SREBP in the liver and a target of Fbxw7-mediated proteolysis (16, 17), was increased both in pIpC-injected *Mx1*-Cre/*Fbxw7*$^{F/F}$ mice and in *Alb*-Cre/*Fbxw7*$^{F/F}$ mice (Figure 3B and Supplemental Figure 2). The intensity of the more slowly migrating band, likely corresponding to the phosphorylated form of SREBP1, was especially increased, consistent with the previous observation that the phosphorylated forms of SREBPs are targeted by Fbxw7 (16–18), as is generally the case for Fbxw7 substrates (11, 34). In contrast, the amounts of ChREBP and PPAR-γ were decreased in the mutant mice compared with those in control animals, suggestive of the operation of a negative feedback loop triggered by triglyceride accumulation. Consistent with this notion, the abundance of *Pparg* mRNA in the liver was increased in SREBP cleavage–activating protein–deficient mice, in which the SREBP pathway is inactivated (38). The levels of PGC-1α and mTOR (total or phosphorylated forms) were unaffected by hepatic deletion of *Fbxw7*.

RT and real-time PCR analysis revealed that the abundance of mRNAs for the adipogenic and lipogenic transcriptional activators *SREBP1c*, *ChREBP*, and *Pparg* was decreased in the Fbxw7-deficient liver (Figure 3C), suggesting that the transcription of these genes is suppressed by a negative feedback loop triggered by the high level of triglyceride. At the protein level, the precursor form of SREBP1 was reduced, probably as a result of the decrease in the abundance of its mRNA, whereas the mature cleaved form was increased (Supplemental Figure 3). Among the downstream targets of SREBPs,

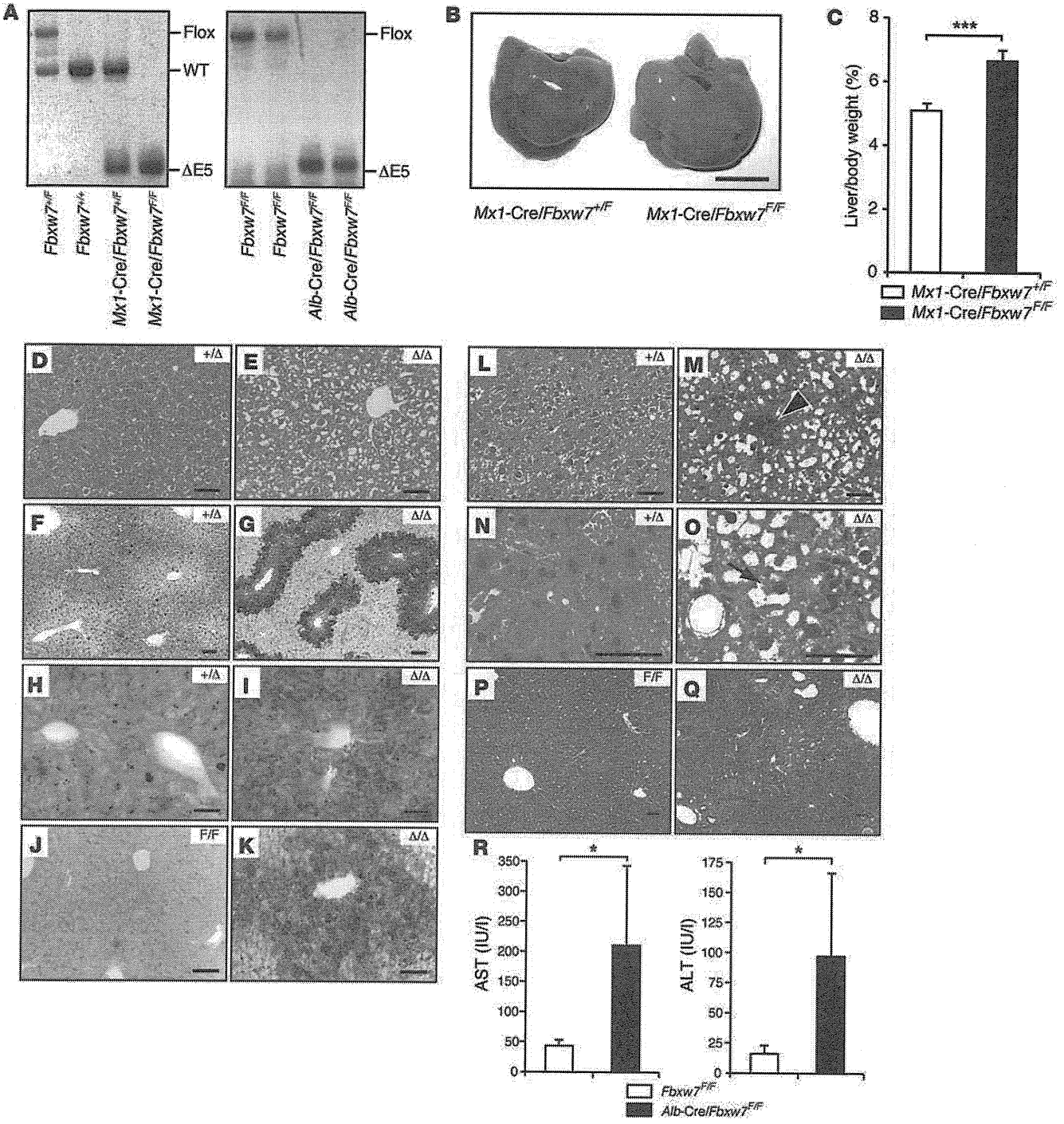

Figure 1

Development of NASH-like liver disease as a result of Fbxw7 deletion. (**A**) Genomic PCR analysis from the mouse liver of the indicated genotypes. The positions of amplified fragments corresponding to WT, floxed, and exon 5–deleted (ΔE5) alleles are indicated. (**B**) Gross appearance of the livers of indicated genotypes treated as in **A**. Scale bar: 10 mm. (**C**) Liver/body weight ratio of mice treated as in **A**. Data are mean ± SD from 5 animals of each genotype. ***$P < 0.005$. (**D** and **E**) H&E staining of liver sections from *Mx1*-Cre/*Fbxw7*$^{+/F}$ (+/Δ) and *Mx1*-Cre/*Fbxw7*$^{F/F}$ (Δ/Δ) mice, respectively, treated as in **A**. (**F** and **G**) Oil red O staining of liver sections treated as in **A**. (**H** and **I**) Higher-magnification views of images in **F** and **G**, respectively. (**J** and **K**) Oil red O staining of liver sections from *Fbxw7*$^{F/F}$ (F/F) and *Alb*-Cre/*Fbxw7*$^{F/F}$ (Δ/Δ) mice, respectively, at 12 weeks of age. (**L**–**O**) H&E staining of liver sections from *Mx1*-Cre/*Fbxw7*$^{+/F}$ (+/Δ) (**L** and **N**) and *Mx1*-Cre/*Fbxw7*$^{F/F}$ (Δ/Δ) (**M** and **O**) mice at 50 weeks after the final injection of pIpC. Lobular infiltration of inflammatory cells is indicated by the arrowhead, and Mallory body–like eosinophilic inclusion is indicated by the arrow. (**P** and **Q**) Masson's trichrome staining of liver sections from *Fbxw7*$^{F/F}$ (F/F) and *Alb*-Cre/*Fbxw7*$^{F/F}$ (Δ/Δ) mice, respectively, at 50 weeks of age. Scale bar: 50 μm (**D**, **E**, **H**, **I**, and **L**–**O**); 100 μm (**F**, **G**, **J**, **K**, **P**, and **Q**). (**R**) Serum AST and ALT activities in *Fbxw7*$^{F/F}$ ($n = 6$) and *Alb*-Cre/*Fbxw7*$^{F/F}$ ($n = 10$) mice at 50 weeks of age. Data are mean ± SD. *$P < 0.05$.

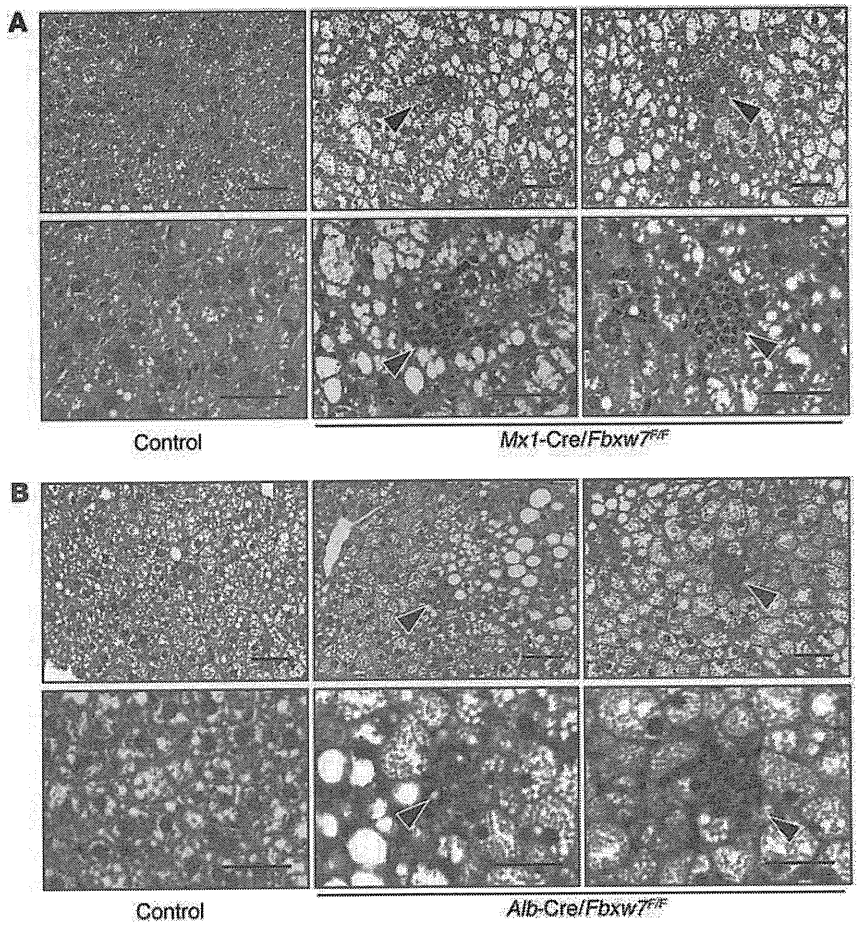

Figure 2
Increased susceptibility to a NASH-like condition conferred by Fbxw7 ablation in the liver. (**A**) *Mx1*-Cre/*Fbxw7*$^{+/F}$ (control) and *Mx1*-Cre/*Fbxw7*$^{F/F}$ mice were injected with pIpC at 8 weeks of age and then fed an MCD diet for 2 weeks. Liver sections were then subjected to H&E staining. Lower- and higher-magnification views are shown (top and bottom panels, respectively). In addition to fatty degeneration, many foci of lobular infiltration of inflammatory cells (arrowheads) were apparent in the livers of *Mx1*-Cre/*Fbxw7*$^{F/F}$ mice. Scale bar: 50 μm. (**B**) *Alb*-Cre/*Fbxw7*$^{+/F}$ (control) and *Alb*-Cre/*Fbxw7*$^{F/F}$ mice at 12 weeks of age were fed an MCD diet for 4 weeks and then analyzed as in **A**. Lower- and higher-magnification views are shown (top and bottom panels, respectively). Control mice developed a small extent of fatty degeneration, whereas *Alb*-Cre/*Fbxw7*$^{F/F}$ mice showed massive accumulation of lipid droplets and many foci of lobular infiltration of inflammatory cells (arrowheads) similar to those apparent in *Mx1*-Cre/*Fbxw7*$^{F/F}$ mice. Scale bar: 50 μm.

the amounts of mRNAs for fatty acid synthase (*Fas*) and stearoyl-CoA desaturase-1 (*Scd1*) were increased, whereas those for the LDL receptor (*Ldlr*) and HMG-CoA synthase (*Hmgcs1*) were decreased, in the mutant liver (Figure 3C). Immunostaining also showed that SREBP1 accumulated in the region around the central veins (Figure 3D), corresponding to the area of lipid deposition, even though deletion of *Fbxw7* appears to occur throughout almost the entire liver. The expression of SCD-1 was also increased in the region around the central veins in which SREBP1 was upregulated (Figure 3E). Collectively, these results suggested that the accumulation of SREBP proteins as a result of Fbxw7 ablation results in triglyceride deposition in the liver, which in turn affects the expression of other adipogenic and lipogenic genes as well as their downstream targets via a negative feedback loop.

Increased proliferation of Fbxw7-deficient hepatocytes. We compared the abundance of cyclin E and c-Myc between the livers of *Mx1*-Cre/*Fbxw7*$^{+/F}$ and *Mx1*-Cre/*Fbxw7*$^{F/F}$ mice at 3 or 50 weeks after the final pIpC injection, beginning at 8 weeks of age. Immunoblot analysis revealed that the amount of cyclin E in the livers of *Mx1*-Cre/*Fbxw7*$^{F/F}$ mice was increased compared with that in *Mx1*-Cre/*Fbxw7*$^{+/F}$ mice at 3 weeks after pIpC injection but not at 50 weeks (Figure 4A). The abundance of c-Myc was not affected by the loss of Fbxw7 in the liver, at either 3 or 50 weeks after injection. To measure the rate of hepatocyte proliferation, we subjected *Mx1*-Cre/*Fbxw7*$^{+/F}$ and *Mx1*-Cre/*Fbxw7*$^{F/F}$ mice to i.p. injection with BrdU for 3 consecutive days, beginning at 3 or 50 weeks after the final pIpC injection. Immunostaining of the liver with antibodies to BrdU at 1 day after the last BrdU injection revealed that the rate of BrdU incorporation was markedly increased in Fbxw7-deficient liver cells compared with that in control cells (Figure 4B). Most of the BrdU-positive cells were also reactive with antibodies to albumin but not with those to cytokeratin 19 (CK19) at 3 weeks after pIpC injection (Figure 4C), suggesting that the proliferating cells are predominantly hepatocytes. In contrast, at 50 weeks after pIpC injection, both hepatocytes and cholangiocytes in *Mx1*-Cre/*Fbxw7*$^{F/F}$ mice incorporated BrdU to a greater extent than did those in control mice. The TUNEL assay revealed that the frequency of apoptosis was also increased in the Fbxw7-deficient liver at 3 weeks after pIpC injection (Figure 4, D and E), suggesting that the loss of Fbxw7 transiently promotes cell cycle progression but eventually results in apoptosis in the liver, as it does in T lymphocytes (34).

Development of hamartomas with hyperproliferation of the biliary system in the Fbxw7-deficient liver. We next examined in more detail the long-term effects of Fbxw7 loss in the liver. Macroscopic examination of *Mx1*-Cre/*Fbxw7*$^{F/F}$ mice at 50 weeks after pIpC injection at 8 weeks of age revealed that the mutant liver was enlarged and darker in color compared with the control liver and possessed a rough surface as a result of the presence of several nodules (Figure 5A). We confirmed that the *Fbxw7* gene was deleted in such nodules (Figure 5B), which were grossly demarcated and readily excised from the liver. Histological examination revealed structural abnormalities characterized by marked dilation of intrahepatic bile ducts as well as apparent proliferation of the biliary system

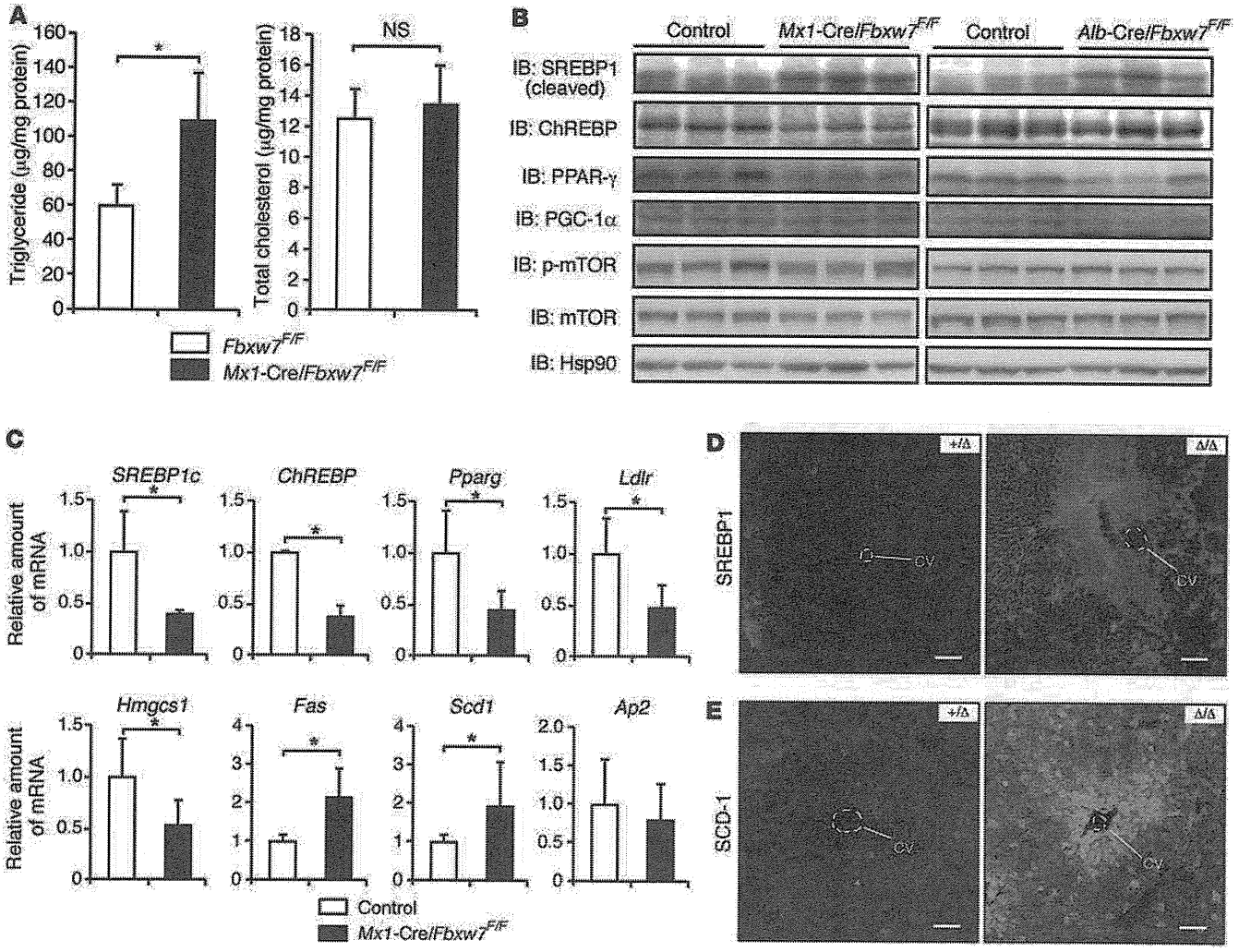

Figure 3

Deposition of triglyceride and accumulation of SREBP1 in the Fbxw7-deficient liver. (**A**) Triglyceride and total cholesterol concentrations in the livers of *Mx1*-Cre/*Fbxw7*$^{+/F}$ (control) and *Mx1*-Cre/*Fbxw7*$^{F/F}$ mice at 3 weeks after the final injection of pIpC, beginning at 8 weeks of age. Data are mean ± SD from 3 mice of each genotype. *$P < 0.05$. (**B**) Protein extracts of the livers of *Mx1*-Cre/*Fbxw7*$^{+/F}$ (control) and *Mx1*-Cre/*Fbxw7*$^{F/F}$ mice at 3 weeks after the final injection of pIpC, beginning at 8 weeks of age, were subjected to IB analysis with antibodies to the indicated proteins (left panel). Liver extracts of *Fbxw7*$^{F/F}$ (control) and *Alb*-Cre/*Fbxw7*$^{F/F}$ mice at 12 weeks of age were similarly analyzed (right panel). Three animals were examined for each genotype. Hsp90 was analyzed as a loading control. p-mTOR, phosphorylated mTOR. (**C**) RT and real-time PCR analysis of the indicated mRNAs in the livers of *Mx1*-Cre/*Fbxw7*$^{+/F}$ (control) and *Mx1*-Cre/*Fbxw7*$^{F/F}$ mice treated as in **A**. Normalized data are expressed relative to the corresponding value for control mice and are mean ± SD from 3 independent experiments. *$P < 0.05$. (**D** and **E**) Liver sections of *Mx1*-Cre/*Fbxw7*$^{+/F}$ (+/Δ) and *Mx1*-Cre/*Fbxw7*$^{F/F}$ (Δ/Δ) mice, treated as in **A**, were subjected to immunofluorescence staining with antibodies (**D**) to SREBP1 and (**E**) to SCD-1. CV, central vein. Scale bar: 100 μm.

(Figure 5, C–F); these abnormalities were pathologically diagnosed as hamartomas. Such lesions were also observed, albeit to a lesser extent, in *Alb*-Cre/*Fbxw7*$^{F/F}$ mice at as early as 12 weeks of age (Figure 5, G and H). Hamartomas, which are reactive with antibodies to CK19 (Figure 5, I and J), developed in all mutant mice of both genotypes examined ($n = 14$). These results suggested that the loss of Fbxw7 may promote proliferation of the biliary system and shift the development of hepatic stem cells toward the cholangiocyte lineage rather than the hepatocyte lineage.

We examined the abundance of mRNAs for *Alb* (Figure 5K) and *CK19* (Figure 5L) as markers of hepatocyte and cholangiocyte lineages, respectively. The amount of *CK19* mRNA in the liver was increased as early as 2 weeks after pIpC injection in *Mx1*-Cre/*Fbxw7*$^{F/F}$ mice and showed a more than 40-fold increase at 50 weeks after *Fbxw7* deletion. In contrast, the abundance of *Alb* mRNA in the mutant liver at 50 weeks after pIpC injection was decreased by 40% compared with that in control liver. These changes in differentiation markers were thus consistent with a marked proliferation of the biliary system in the Fbxw7-deficient liver.

Skewed hepatic differentiation induced by Notch1 accumulation in the Fbxw7-deficient liver. The hepatic cell fate decision is thought to be largely dependent on Notch signaling (39–44). We therefore examined the expression of Notch, a target of Fbxw7, in the Fbxw7-deficient liver. Although immunoblot analysis did not reveal an

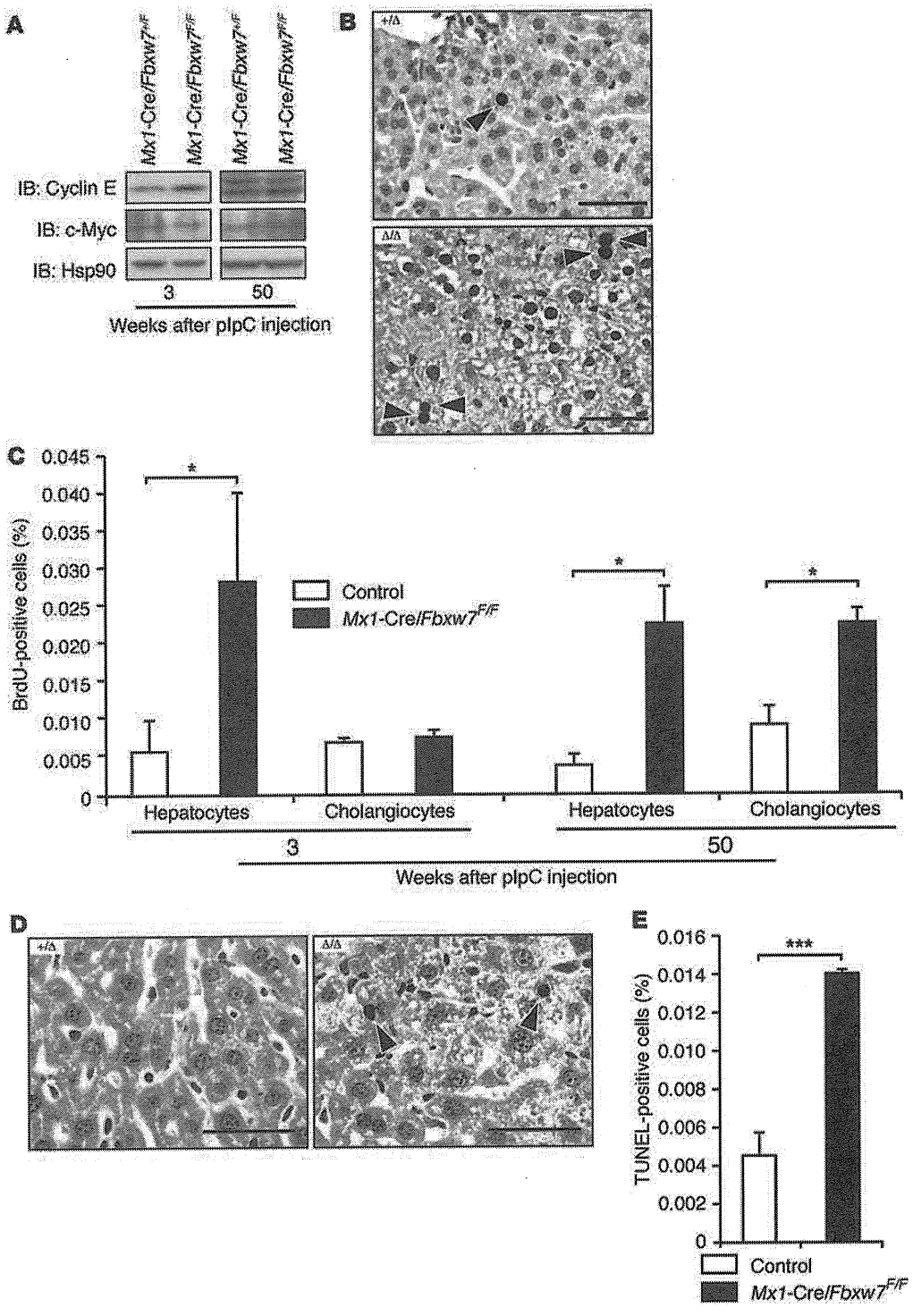

Figure 4
Increased proliferation and apoptosis of Fbxw7-deficient hepatocytes. (**A**) IB analysis of cyclin E, c-Myc, and Hsp90 (loading control) in liver extracts from *Mx1*-Cre/*Fbxw7*$^{+/F}$ and *Mx1*-Cre/*Fbxw7*$^{F/F}$ mice at 3 or 50 weeks after *Fbxw7* deletion by pIpC injection, beginning at 8 weeks of age. (**B**) Representative immunostaining for BrdU in liver sections from *Mx1*-Cre/*Fbxw7*$^{+/F}$ (+/Δ) and *Mx1*-Cre/*Fbxw7*$^{F/F}$ (Δ/Δ) mice injected with BrdU on 3 consecutive days, beginning 3 weeks after the final pIpC injection as in **A**. Arrowheads indicate BrdU-positive nuclei. Scale bar: 50 μm. (**C**) The proportion of BrdU-positive hepatocytes or cholangiocytes was determined from immunostaining for BrdU in combination with that for albumin or CK19 in the livers of *Mx1*-Cre/*Fbxw7*$^{+/F}$ (control) or *Mx1*-Cre/*Fbxw7*$^{F/F}$ mice at 3 or 50 weeks after deletion of *Fbxw7* as in **A**. Data are mean ± SD from 10 fields from 3 mice of each genotype. *$P < 0.05$. (**D**) Representative TUNEL staining for liver sections of *Mx1*-Cre/*Fbxw7*$^{+/F}$ (+/Δ) and *Mx1*-Cre/*Fbxw7*$^{F/F}$ (Δ/Δ) mice 3 weeks after the final pIpC injection as in **A**. Arrowheads indicate TUNEL-positive cells. Scale bar: 50 μm. (**E**) The proportion of TUNEL-positive liver cells was determined from images similar to those in **D**. Data are mean ± SD from 3 animals of each genotype. ***$P < 0.005$.

increase in the abundance of any of the isoforms of Notch in the liver of *Mx1*-Cre/*Fbxw7*$^{F/F}$ mice at either 3 or 50 weeks after *Fbxw7* deletion (data not shown), confocal microscopic analysis revealed that the intracellular domain of Notch1 was highly concentrated in both the cytoplasm and the nucleus of Fbxw7-deficient liver at 3 weeks after pIpC injection (Figure 6A). Consistent with the observed upregulation of Notch1, the abundance of Notch1 target genes, including those for Hes1 and Hey1, was simultaneously increased in the livers of *Mx1*-Cre/*Fbxw7*$^{F/F}$ mice (Figure 6B and Supplemental Figure 5A, respectively). At 15 weeks after pIpC injection, Notch1 accumulated in the hepatocyte-like cells residing around the portal area, and these cells were reactive to antibodies to CK7 (Figure 6C), another marker of cholangiocytes, suggesting that such cells might be in the process of transdifferentiation to the cholangiocytes by Notch activation. At 50 weeks after pIpC injection, Notch1 was observed in the form of aggregates in the

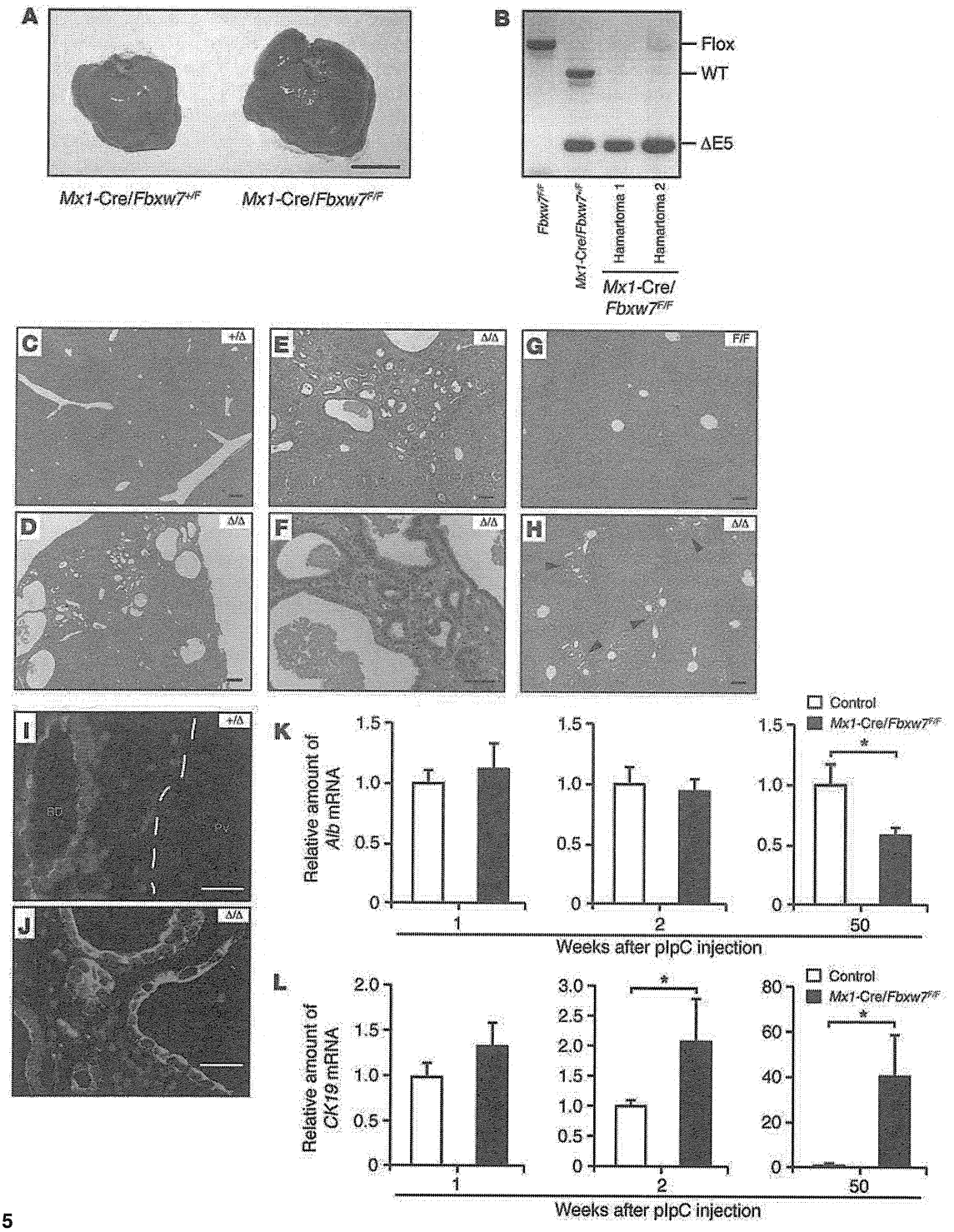

Figure 5

Hamartoma development as a result of long-term ablation of Fbxw7 in the liver. (**A**) Gross appearance of the livers of *Mx1*-Cre/*Fbxw7*$^{+/F}$ and *Mx1*-Cre/*Fbxw7*$^{F/F}$ mice at 50 weeks after the final injection of pIpC, beginning at 8 weeks of age. Scale bar: 10 mm. (**B**) PCR analysis of genomic DNA from the dilated bile ducts excised from hamartomas in the livers of 2 *Mx1*-Cre/*Fbxw7*$^{F/F}$ mice. Genomic DNA from control mice was also analyzed. (**C**–**F**) H&E staining of liver sections from a *Mx1*-Cre/*Fbxw7*$^{+/F}$ (+/Δ) mouse (**C**) and from a *Mx1*-Cre/*Fbxw7*$^{F/F}$ (Δ/Δ) mouse (**D**–**F**) that developed hamartoma after *Fbxw7* deletion as in **A**. (**G** and **H**) H&E staining of liver sections from *Fbxw7*$^{F/F}$ (F/F) and *Alb*-Cre/*Fbxw7*$^{F/F}$ (Δ/Δ) mice, respectively, at 12 weeks of age. Arrowheads indicate malformation of the ductal plate. Scale bar: 50 μm (**F**); 100 μm (**E**, **G**, and **H**); 200 μm (**C** and **D**). (**I** and **J**) Immunofluorescence staining for CK19 in the livers of *Mx1*-Cre/*Fbxw7*$^{+/F}$ (+/Δ) and *Mx1*-Cre/*Fbxw7*$^{F/F}$ (Δ/Δ) mice at 50 weeks after the final injection of pIpC, beginning at 8 weeks of age. The dashed line indicates the outer boundary of portal vein. PV, portal vein; BD, bile duct. Scale bar: 25 μm. (**K** and **L**) RT and real-time PCR analysis of *Alb* and *CK19* mRNAs, respectively, in the livers of *Mx1*-Cre/*Fbxw7*$^{+/F}$ (control) and *Mx1*-Cre/*Fbxw7*$^{F/F}$ mice at 1, 2, or 50 weeks after deletion of *Fbxw7* as in **A**. Normalized data are expressed relative to the corresponding value for control mice. Data are mean ± SD from 3 independent experiments. *$P < 0.05$.